JCB Journal of Cell Biology

ARTICLE

WDR60-mediated dynein-2 loading into cilia powers retrograde IFT and transition zone crossing

Ana R.G. De-Castro[1,2*], Diogo R.M. Rodrigues[1,2,3*], Maria J.G. De-Castro[1,2], Neide Vieira[4,5], Cármen Vieira[1,2], Ana X. Carvalho[1,2], Reto Gassmann[1,2], Carla M.C. Abreu[1,2], and Tiago J. Dantas[1,2]

The dynein-2 motor complex drives retrograde intraflagellar transport (IFT), playing a pivotal role in the assembly and functions of cilia. However, the mechanisms that regulate dynein-2 motility remain poorly understood. Here, we identify the *Caenorhabditis elegans* WDR60 homologue, WDR-60, and dissect the roles of this intermediate chain using genome editing and live imaging of endogenous dynein-2/IFT components. We find that loss of WDR-60 impairs dynein-2 recruitment to cilia and its incorporation onto anterograde IFT trains, reducing retrograde motor availability at the ciliary tip. Consistent with this, we show that fewer dynein-2 motors power WDR-60–deficient retrograde IFT trains, which move at reduced velocities and fail to exit cilia, accumulating on the distal side of the transition zone. Remarkably, disrupting the transition zone's NPHP module almost fully restores ciliary exit of underpowered retrograde trains in *wdr-60* mutants. This work establishes WDR-60 as a major contributor to IFT, and the NPHP module as a roadblock to dynein-2 passage through the transition zone.

Introduction

Cilia are microtubule-based structures that project outward from the surface of most mammalian cell types. These antenna-like structures can produce mechanical force for locomotion or fluid flow (such as in the multiciliated airway epithelia) or sense extracellular signals that modulate developmental pathways, ultimately regulating cell proliferation and differentiation (Drummond, 2012). Regardless of their type, the assembly and functions of cilia depend on a bidirectional transport system known as intraflagellar transport (IFT; Kozminski et al., 1993; Prevo et al., 2017; Webb et al., 2020). IFT is driven by two classes of molecular motors that travel on the ciliary microtubules that compose the axoneme. Kinesin-2 motors cooperate with both IFT-B and IFT-A complexes to power the transport of cargos in the anterograde direction from the base to the tip of cilia (Kozminski et al., 1995; Prevo et al., 2017). In the opposite direction, cytoplasmic dynein-2 motors (hereafter referred to as dynein-2) associate with the IFT-A complex to drive retrograde transport (Pazour et al., 1999; Porter et al., 1999; Wicks et al., 2000), which is critical for the retrieval of signaling molecules and the recycling of ciliary proteins (Prevo et al., 2017; Webb et al., 2020).

Between the base and the axoneme of cilia, a specialized ciliary gate known as the transition zone (TZ) controls which proteins and membrane components enter and exit the cilium, thus isolating the ciliary environment from the cytoplasm (Garcia-Gonzalo and Reiter, 2017). The assembly and gating function of the TZ is a complex process that involves many soluble and membrane-bound components organized into the MKS (Meckel–Gruber syndrome) and NPHP (nephronophthisis) modules (Garcia-Gonzalo and Reiter, 2017). These two modules cooperate for the building of Y-shaped structures (Y-links) that connect the proximal end of the axonemal doublets to the ciliary membrane at the region of the ciliary necklace (Blacque and Sanders, 2014). At the center of the TZ lies an apical ring (or central cylinder) that also contributes to the integrity and gating of the TZ (Li et al., 2016; Schouteden et al., 2015). Interestingly, dynein-2 has been recently shown to be required for the stability of the TZ (Jensen et al., 2018; Vuolo et al., 2018).

Problems in IFT or in the integrity of the TZ result in defects in cilia assembly/functions that can lead to congenital developmental diseases, collectively known as ciliopathies (Drummond, 2012; Garcia-Gonzalo and Reiter, 2017). Mutations in genes coding for dynein-2 subunits are associated with severe skeletal dysplasias such as Jeune syndrome (asphyxiating thoracic dystrophy), Ellis–van Creveld syndrome, and short-rib polydactyly syndrome (SRPS), which in many cases are incompatible with

[1]i3S - Instituto de Investigação e Inovação em Saúde, Universidade do Porto, Porto, Portugal; [2]IBMC - Instituto de Biologia Molecular e Celular, Universidade do Porto, Porto, Portugal; [3]Instituto de Ciências Biomédicas Abel Salazar (ICBAS), Universidade do Porto, Porto, Portugal; [4]Life and Health Sciences Research Institute (ICVS), School of Medicine, University of Minho, Campus Gualtar, Braga, Portugal; [5]ICVS/3B's - PT Government Associate Laboratory, Braga/Guimarães, Portugal.

*A.R.G. De-Castro and D.R.M. Rodrigues contributed equally to this paper; Correspondence to Carla M.C. Abreu: carla.abreu@ibmc.up.pt; Tiago J. Dantas: tiago.dantas@i3s.up.pt.

© 2021 De-Castro et al. This article is distributed under the terms of an Attribution–Noncommercial–Share Alike–No Mirror Sites license for the first six months after the publication date (see http://www.rupress.org/terms/). After six months it is available under a Creative Commons License (Attribution–Noncommercial–Share Alike 4.0 International license, as described at https://creativecommons.org/licenses/by-nc-sa/4.0/).

Downloaded from http://rupress.org/jcb/article-pdf/221/1/e202010178/1818538/jcb_202010178.pdf by guest on 10 February 2026

fetal survival (Cossu et al., 2016; Dagoneau et al., 2009; Huber et al., 2013; McInerney-Leo et al., 2013; Merrill et al., 2009; Niceta et al., 2018; Schmidts et al., 2015; Schmidts et al., 2013; Taylor et al., 2015). How mutations in dynein-2 subunits lead to these disorders remains poorly understood.

Dynein-2 is a giant (>1 MDa) motor protein complex composed of heavy chains (HCs), intermediate chains (ICs), light intermediate chains (LICs), and light chains (Toropova et al., 2019). A homodimer of two HCs (DHC2 encoded by *DYNC2H1*) makes up the core of the motor complex. Each DHC2 has an N-terminal tail that serves as a platform for the binding of other subunits, and a C-terminus (CT) comprising six AAA ATPase domains and a microtubule-binding domain that enable dynein-2 movement on microtubules. Two copies of the dynein-2–specific LIC3 (encoded by *DYNC2LI1*) bind and serve to stabilize the DHC2s (Mikami et al., 2002; Taylor et al., 2015; Toropova et al., 2019). The DHC2-LIC3 subcomplex binds a heterodimer of ICs, composed of WDR60 and WDR34 (encoded by *DYNC2I1* and *DYNC2I2*, respectively), through their CT β-propeller domains (Asante et al., 2014; Patel-King et al., 2013; Rompolas et al., 2007; Toropova et al., 2019). In turn, the WDR60-WDR34 heterodimer is stabilized through the binding of multiple light chains at their N-terminus (NT; Hamada et al., 2018; Schmidts et al., 2015; Toropova et al., 2019; Tsurumi et al., 2019).

Recent work analyzing the effects of depleting or disrupting the WDR60/WDR34 ICs in human cells has yielded inconsistent results, particularly regarding the requirement of WDR60 for ciliogenesis and cilia axoneme length control (Asante et al., 2014; Hamada et al., 2018; McInerney-Leo et al., 2013; Vuolo et al., 2018). Importantly, the impact of WDR60 loss on dynein-2 activity and dynamics during IFT has not been determined. This in part is due to the difficulty in visualizing and quantifying IFT kinetics of dynein-2 subunits (especially of DHC2) inside cilia of cultured cells (Hamada et al., 2018; Taylor et al., 2015; Vuolo et al., 2018).

In *Caenorhabditis elegans*, GFP/RFP-tagged dynein-2 HC and LIC subunits (see Table S1 for nomenclature) are readily detectable inside cilia and easy to track during IFT (Mijalkovic et al., 2017; Schafer et al., 2003; Yi et al., 2017). Another advantage of this model is that mutations in dynein-2 subunits that are lethal in mice (Huangfu and Anderson, 2005; May et al., 2005; Rana et al., 2004; Wu et al., 2017) do not compromise viability in *C. elegans* (Schafer et al., 2003; Wicks et al., 2000; Yi et al., 2017). Cilia are only present in a subset of *C. elegans* sensory neurons, which are analogous to human sensory cilia, such as those present in olfactory neurons. Despite being dispensable for survival, *C. elegans* cilia have key sensory functions that modulate easily quantifiable animal behaviors in response to environmental cues (Bae and Barr, 2008). These features make *C. elegans* a powerful model to dissect the roles of dynein-2 subunits during IFT.

Although most dynein-2 core subunits have been identified in *C. elegans*, clear homologues of WDR34 and WDR60 have remained unknown (Vuolo et al., 2020). Here, we identify the *C. elegans* WDR60 homologue, WDR-60, and dissect its contribution to ciliary recruitment of dynein-2 subunits, retrograde IFT, and cilia-mediated behavior. Using CRISPR/Cas9-mediated genome editing, we tagged endogenous WDR-60 with GFP and tracked its dynamics during IFT in cilia of sensory neurons. In addition, we generated a strain expressing an SRPS patient-equivalent WDR-60 truncation (McInerney-Leo et al., 2013) that lacks the DHC2-binding β-propeller domain (Toropova et al., 2019), and compared this mutant with a *wdr-60(null)* mutant. We show that WDR-60 is mostly dispensable for axoneme extension but is required for efficient loading of dynein-2 onto anterograde IFT trains, for reaching maximum retrograde IFT velocity, and for dynein-2 crossing of the TZ to exit cilia. By targeting specific TZ components, we were able to facilitate dynein-2 exit from WDR-60–deficient cilia, showing that dynein-2 is unable to overcome the resistance offered by the TZ barrier in the absence of WDR-60.

Results

WDR-60 is recruited to cilia in *C. elegans* sensory neurons and undergoes IFT with kinetics similar to those of dynein-2 HC

We set out to identify the gene encoding the so-far uncharacterized homologue of WDR60 in *C. elegans* (Hou and Witman, 2015; Vuolo et al., 2020). Through protein sequence alignments, we found that the *C27F2.1* gene in *C. elegans* encodes the protein with the highest sequence homology to human WDR60. Interestingly, *C27F2.1* (hereafter referred to as *wdr-60*) was one of the early candidate genes identified in a screen for transcripts specific for ciliated sensory neurons (Blacque et al., 2005). Like genes encoding for other dynein-2 subunits (Swoboda et al., 2000), *wdr-60* contains a predicted X-box sequence (Fig. S1 A), which is a target of the regulatory factor X (RFX)-like transcription factor DAF-19 (Blacque et al., 2005).

To directly visualize and analyze the dynamics of the protein encoded by *wdr-60*, we used genome editing to introduce the coding sequence for a 3xFLAG::GFP tag at the endogenous *wdr-60* locus (Fig. S1 A). Similar to what has been described for dynein-2 LIC and HC (Schafer et al., 2003; Wicks et al., 2000), we found that WDR-60 expression is restricted to ciliated sensory neurons. To better define the tissue-specific expression of WDR-60, we performed the classic dye filling assay that takes advantage of a lipophilic fluorescent dye (DiI) that is specifically incorporated into ciliated sensory neurons that have their cilia in contact with the environment. As a control, we used a GFP knock-in strain of dynein-2 HC, GFP::CHE-3 (Yi et al., 2017). We found that the expression pattern of WDR-60::3xFLAG::GFP is identical to that of GFP::CHE-3 and perfectly matches the neurons that take up dye (Fig. 1 A). While a large part of the signal is detected in the soma and dendrites of these neurons, WDR-60 is also found inside cilia, similar to what has been observed for GFP::CHE-3 (Yi et al., 2017).

When analyzing WDR-60::GFP ciliary distribution in more detail, we found that WDR-60 is particularly enriched at the ciliary base, as is the case for GFP::CHE-3 (Fig. 1, B–E). Furthermore, both subunits colocalize with dynein-2 LIC, XBX-1::RFP (Yi et al., 2017). Next, we performed time-lapse imaging to gain insight into WDR-60 dynamics (Video 1). We found that both anterograde and retrograde frequencies (Fig. 1, F and G) and velocities (Fig. 1, H–K) of WDR-60::GFP particles match

Downloaded from http://rupress.org/jcb/article-pdf/221/1/e202010178/1818538/jcb_202010178.pdf by guest on 10 February 2026

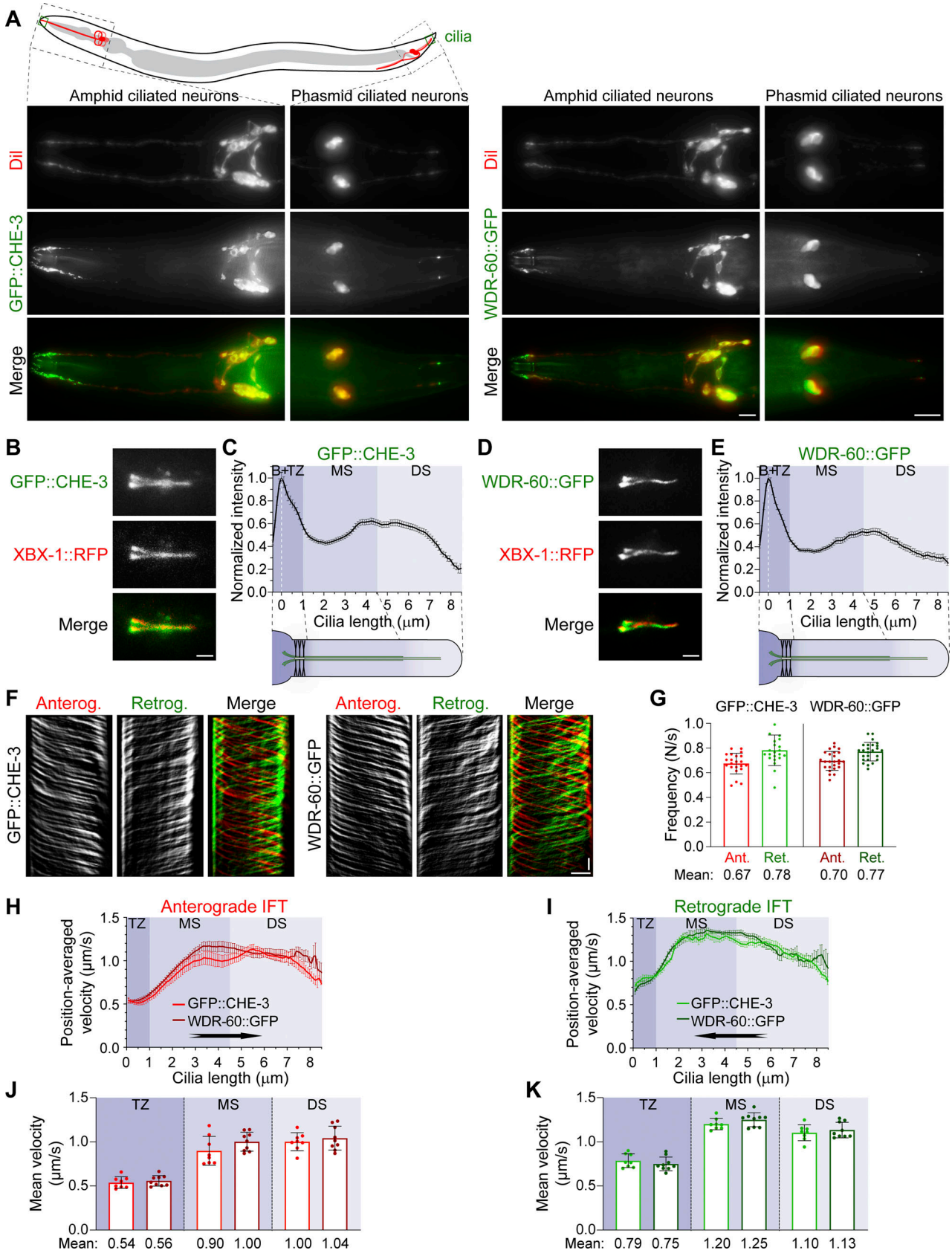

Figure 1. **WDR-60 expression is restricted to ciliated sensory neurons, where it has distribution and IFT kinetics similar to those of dynein-2 HC.** **(A)** Endogenously tagged WDR-60::3xFLAG::GFP is expressed in the same ciliated neurons that express dynein-2 HC (GFP::CHE-3). These are the same neurons that incorporate the DiI lipophilic dye. The top illustration shows the relative localization of amphid and phasmid ciliated neurons in *C. elegans*. **(B)** Phasmid cilia

Downloaded from http://rupress.org/jcb/article-pdf/221/1/e202010178/1818538/jcb_202010178.pdf by guest on 10 February 2026

coexpressing GFP::CHE-3 and XBX-1::RFP. **(C)** Quantification of GFP::CHE-3 signal intensity along cilia (n = 109 cilia). **(D)** Phasmid cilia coexpressing WDR-60::3xFLAG::GFP and XBX-1::RFP. **(E)** Quantification of WDR-60::3xFLAG::GFP signal intensity along cilia (n = 101 cilia). **(F)** Cilium kymographs of GFP::CHE-3 and WDR-60::3xFLAG::GFP. Single and merge channels for particles moving anterogradely and retrogradely are shown. **(G)** Mean IFT frequency of anterogradely and retrogradely moving GFP::CHE-3 and WDR-60::3xFLAG::GFP particles per second ($n \geq 22$ cilia). **(H and I)** Anterograde and retrograde velocities of GFP::CHE-3 and WDR-60::3xFLAG::GFP particles along cilia. **(J and K)** Mean velocities for each cilium subcompartment ($n \geq 430$ particle traces were analyzed in ≥ 8 cilia). B, cilium base; TZ, transition zone; MS, middle segment; DS, distal segment. XY velocity and intensity distribution graphs are shown as mean ± SEM, and graphs in columns are shown as mean ± SD. Student' t test was used to analyze the datasets in G, J, and K. Scale bars: 10 µm (A); 2 µm (B and D); vertical 5 s, horizontal 2 µm (F).

those of GFP::CHE-3. Furthermore, retrograde WDR-60::GFP motility follows a triphasic model, as previously reported for GFP::CHE-3 (Yi et al., 2017; Fig. 1, I and K). Together, these data strongly support that *C27F2.1/wdr-60* encodes for the *C. elegans* WDR60 homologue, which undergoes IFT with kinetics that resemble those of dynein-2 HC.

The β-propeller domain is important but not essential for WDR-60 incorporation into cilia

To determine the importance of WDR-60 for dynein-2–mediated IFT and cilia assembly, we first characterized WDR-60 levels and distribution in two distinct *wdr-60* mutants. We took advantage of the available *wdr-60* deletion allele *tm6453* (Fig. S1 B), a null mutation, and we engineered a *wdr-60* allele that produces a truncated form of WDR-60 specifically lacking the CT β-propeller domain (ΔCT; Figs. S1 C and 2 A), required for dynein-2 HC binding (Toropova et al., 2019). The *wdr-60(ΔCT)* mutant mimics a truncating mutation found in an SRPS patient (*WDR60*: c.1891C>T; p.Q631*; McInerney-Leo et al., 2013).

As endogenous labeling of WDR-60 did not alter IFT kinetics (Fig. 1, G–K), we inserted the same 3xFLAG::GFP tag sequence in-frame with the 3′ end of both *wdr-60* mutants (Figs. S1 A and 2 A). Together with the dye-filling assay, this allowed us to analyze the overall integrity of cilia while comparing the neuronal localization and relative levels of WDR-60 in wild-type and in each mutant (Fig. S2, A and B). Interestingly, and in contrast to the null *xbx-1(ok279)* LIC mutant, both *wdr-60* mutants had all ciliated sensory neurons stained with DiI, suggesting that sensory cilia can form and take up dye. No GFP signal was detectable in sensory neurons or in cilia of the *wdr-60(tm6453)* mutant, indicating that no WDR-60 is produced in this strain. In contrast, the GFP signal in neurons of the *wdr-60(ΔCT)* mutant was readily visible and overlapped with the neuronal pattern of the dye (Fig. S2, A and B; and Fig. 2 B). Interestingly, the ciliary signal of WDR-60(ΔCT)::GFP was overall weaker than in controls (approximately threefold reduction; Fig. 2 C) but showed a similar distribution profile along the axoneme, suggesting that a fraction of WDR-60(ΔCT) is able to enter cilia and undergo IFT. Strikingly, although dynein-2 LIC stabilizes the HC (Blisnick et al., 2014; Hou et al., 2004; Reck et al., 2016; Taylor et al., 2015) and contributes to ciliary entry of dynein-2 by directly interacting with IFT-B (Zhu et al., 2021), XBX-1 loss did not significantly affect the ciliary recruitment of WDR-60::GFP or WDR-60(ΔCT)::GFP (Fig. 2, B and C). However, it did lead to the accumulation of both forms of WDR-60 inside cilia, likely due to the complete block of retrograde IFT that occurs in the *xbx-1(null)* mutant (Schafer et al., 2003; Yi et al., 2017). We conclude that WDR-60 can be recruited to cilia independently of dynein-2 LIC and HC subunits.

Taking advantage of the 3xFLAG epitope in our tag, we performed immunoblotting to determine whether the reduction in ciliary levels of mutant WDR-60 reflected differences in overall protein levels (Fig. 2 D). Given that no protein bands were detectable in *wdr-60(tm6453)* worm extracts, we conclude that this mutant strain is indeed a *wdr-60* null. In contrast, the levels of WDR-60(ΔCT)::GFP were comparable to those of full-length WDR-60::GFP, indicating that the reduced ciliary recruitment of WDR-60(ΔCT)::GFP is due to loss of the β-propeller rather than a down-regulation of protein levels.

Disruption of WDR-60 reduces dynein-2 loading into cilia and the kinetics of retrograde IFT

Loss of the dynein-2 LIC XBX-1 destabilizes the dynein-2 HC CHE-3, completely abolishing its recruitment to cilia, blocking retrograde IFT and, consequently, axoneme extension. The resulting cilia are severely truncated and bulged (Schafer et al., 2003; Yi et al., 2017). To directly assess the impact of WDR-60 disruption on cilia and other dynein-2 subunits, we crossed the *wdr-60* mutants with knock-in strains of GFP::CHE-3/XBX-1::RFP (Yi et al., 2017) and analyzed their ciliary recruitment and distribution. While both *wdr-60* mutants were capable of assembling seemingly normal cilia (with only a minor reduction in length in the *wdr-60(null)* mutant), we observed a strong reduction in the total levels of ciliary GFP::CHE-3 (~40%; Fig. 3, A–C). Interestingly, we also found that the remaining pool of WDR-60–deficient dynein-2 accumulated particularly near the ciliary base (Fig. 3 D). Considering that GFP::CHE-3 levels were not greatly altered in the soma of the ciliated phasmid neurons of *wdr-60* mutants (Fig. S2 C), these observations suggest that WDR-60 contributes to both recruitment and ciliary distribution of dynein-2.

To determine when these WDR-60–associated phenotypes start manifesting and whether they vary with aging, we repeated our analysis of GFP::CHE-3 recruitment and distribution in developing and post-adulthood animals. We found that, as early as larval stage 2 in the *wdr-60(null)* mutant, ciliary levels of GFP::CHE-3 were already reduced and its distribution altered, albeit to a lesser degree than in young adults. This suggests that WDR-60–associated dynein-2 phenotypes arise early on and become progressively worse as the mutant animals develop (Fig. S3). In addition, we found that the abnormal distribution of GFP::CHE-3 does not significantly change with age in *wdr-60(null)* animals (7 and 18 days after adulthood; Fig. S3, C–H), suggesting that there is no age-dependent suppression of these WDR-60–associated phenotypes, in contrast to what has been observed for some IFT mutants (Cornils et al., 2016).

To gain further insight into the importance of WDR-60 for dynein-2 loading and dynamics inside cilia, we analyzed the IFT kinetics of GFP::CHE-3 by time-lapse imaging (Fig. 3, E–H; and

Downloaded from http://rupress.org/jcb/article-pdf/221/1/e202010178/1818538/jcb_202010178.pdf by guest on 10 February 2026

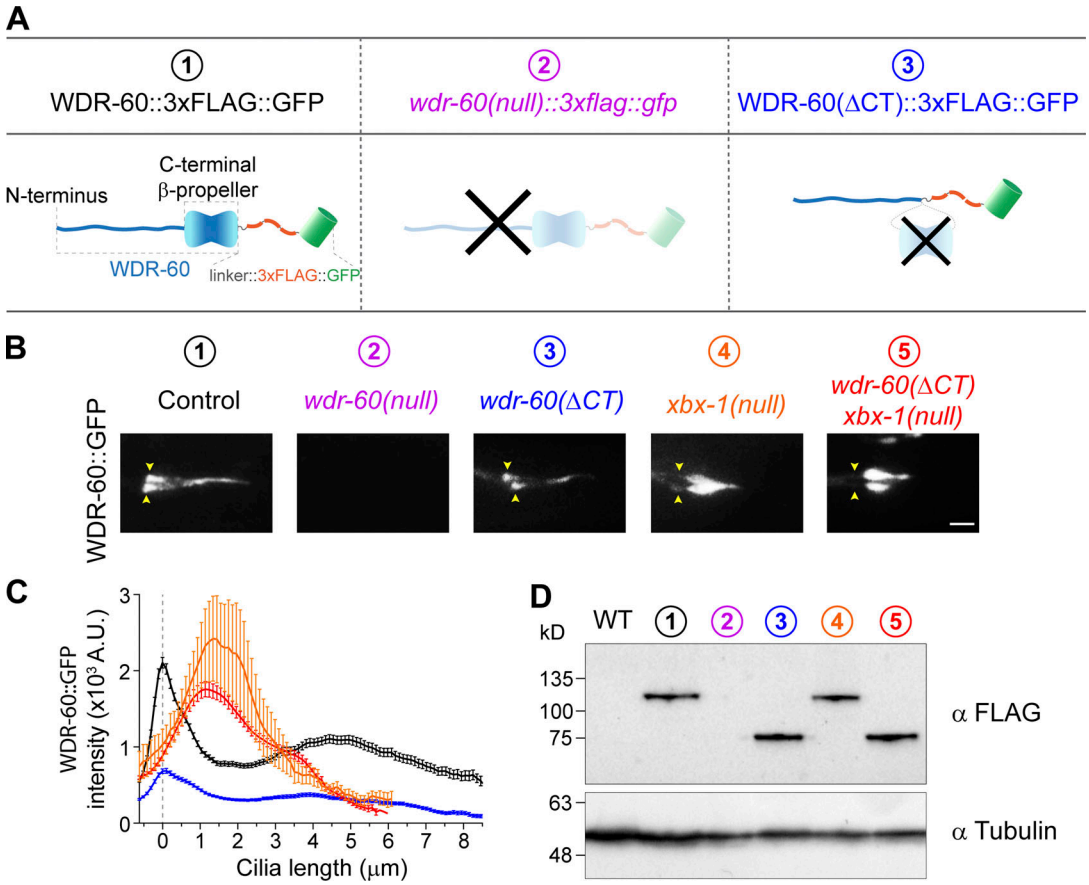

Figure 2. **Truncation of the β-propeller domain reduces, but does not abolish, entry of WDR-60 into cilia. (A)** Schematic representation of WDR-60 tagging with 3xFLAG::GFP in control, *wdr-60(tm6453)* null, and truncated *wdr-60* knock-in strains: (1) full-length WDR-60, composed of an NT disordered region and a CT β-propeller domain; (2) *wdr-60(tm6453)*, predicted to be a null mutant; (3) *wdr-60(ΔCT)*, expected to produce a protein composed of the WDR-60 NT fused to the 3xFLAG::GFP tag (lacking the β-propeller). **(B)** Phasmid cilia of each *wdr-60* knock-in strain as indicated. Yellow arrowheads indicate the ciliary base. Note that no GFP signal is detected in the *wdr-60(tm6453)::3xflag::gfp* strain. Scale bar, 2 µm. **(C)** Quantification of GFP signal intensity distribution along the cilium in *wdr-60* mutants shown in B ($n \geq 55$ cilia). Graph is shown as mean ± SEM. **(D)** Western blot of extracts from wild-type and *wdr-60* knock-in strains using an anti-FLAG antibody. The predicted sizes are 105.6 kD for WDR-60::3xFLAG::GFP and 63.2 kD for WDR-60(ΔCT)::3xFLAG::GFP truncation. No signal is detected in *wdr-60(tm6453)::3xflag::gfp* extracts, demonstrating that this is indeed a null strain. α-Tubulin was used as a loading control. Source data are available for this figure: SourceData F2.

Video 2). While we found a small increase in the frequency of GFP::CHE-3 particles moving in the anterograde direction in the *wdr-60(null)* mutant, the number of particles in the retrograde direction was significantly reduced in both mutants (~15%; Fig. 3 F). Importantly, we found that both the loss of WDR-60 and the truncation of its β-propeller led to a strong reduction in the average amount of GFP::CHE-3 transported on anterograde tracks (~67%; Fig. 3 G). This establishes a role for WDR-60 in the loading of dynein-2 onto anterograde IFT trains. Consistent with this, we found that the intensity of GFP::CHE-3 moving on retrograde tracks was significantly reduced in both *wdr-60* mutants, suggesting that each retrograde IFT train is being powered by fewer dynein-2 motors. In addition, while the velocity of anterograde trains carrying GFP::CHE-3 remained similar to that of controls, we observed a strong reduction in the velocity of GFP::CHE-3-driven retrograde trains in both *wdr-60* mutants (three- to fourfold; Fig. 3 H).

Taken together, these results show that loss of WDR-60 or truncation of its β-propeller reduces the loading of dynein-2 HC onto anterograde IFT trains, and consequently the pool of dynein-2 available at the tip of cilia to power retrograde IFT. In agreement, fewer dynein-2 motors were present in particles moving retrogradely, which may explain the reduced kinetics of retrograde IFT in *wdr-60* mutants and the inability of dynein-2 to fully return to the ciliary base.

WDR-60 is required for efficient recycling of IFT components and contributes to cilia-mediated behavior

To better understand the importance of WDR-60 in IFT, we analyzed fluorescently labeled subunits of the IFT-A/B complexes (Fig. 4, A–F) and anterograde kinesins (Fig. S4, B and C). Measurements of cilia expressing CHE-11::mCherry (IFT140) or IFT-74::GFP confirmed the small but significant decrease in cilium length in the *wdr-60(null)* mutant (Fig. 4, A, B, D, and E). We note, however, that this minor defect in axoneme extension is distinct from the severely shortened and bulged cilia phenotype caused by XBX-1 loss (Fig. 4, A and D).

When analyzing the ciliary distribution of CHE-11::mCherry, we found that this IFT-A component accumulated predominantly near the ciliary base in both *wdr-60* mutants (Fig. 4, A and C),

Downloaded from http://rupress.org/jcb/article-pdf/221/1/e202010178/1818538/jcb_202010178.pdf by guest on 10 February 2026

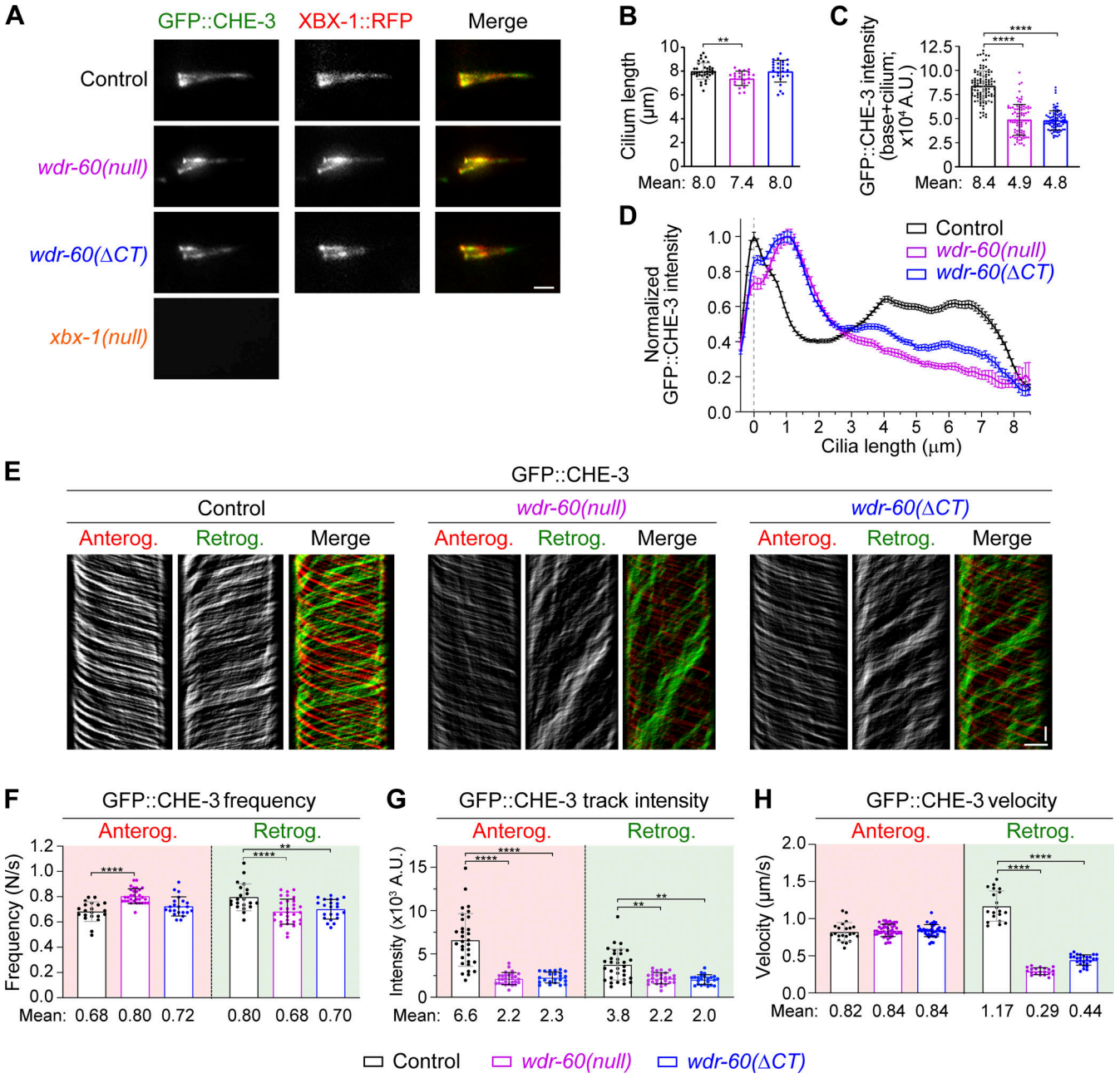

Figure 3. ***wdr-60* mutants have reduced dynein-2 recruitment and incorporation into cilia, accompanied by impaired retrograde IFT. (A)** Phasmid cilia coexpressing GFP::CHE-3 and XBX-1::RFP. **(B)** Cilia length in *wdr-60* mutants ($n \geq 24$ cilia). **(C and D)** Total signal intensity of GFP::CHE-3 from the base to the tip of cilia (C) and relative distribution of GFP::CHE-3 along cilia (D; $n \geq 88$ cilia). **(E)** GFP::CHE-3 kymographs of phasmid cilia of the indicated strains. Single and merge channels for particles moving anterogradely and retrogradely are shown. **(F)** Frequency of IFT particles detected at the distal segment of cilia ($n \geq 20$ cilia). **(G)** Quantification of the average intensity of GFP::CHE-3 particles moving on anterograde and retrograde tracks ($n \geq 345$ particle traces were analyzed in ≥23 cilia). **(H)** Velocity of anterograde and retrograde GFP::CHE-3 particles in control and *wdr-60* mutants ($n \geq 300$ particle traces were analyzed in ≥20 cilia). XY intensity distribution graph is shown as mean ± SEM, and graphs in columns are shown as mean ± SD. One-way ANOVA followed by Dunnett's, Holm–Sidak, and Games–Howell multiple comparison were used to analyze the datasets in B, F, and G, respectively. Kruskal–Wallis test followed by Dunn's multiple comparison were used to analyze the datasets in C and H. **, $P \leq 0.01$; ****, $P \leq 0.0001$. Scale bars: 2 μm (A); vertical 5 s, horizontal 2 μm (E).

similar to our observations with GFP::CHE-3. Interestingly, the total levels of CHE-11::mCherry retained inside cilia were substantially higher in the *wdr-60(null)* mutant when compared with the *wdr-60(ΔCT)* mutant.

Consistent with defects in dynein-2 function, we found that the retrograde velocity of CHE-11::mCherry was strongly reduced in both *wdr-60* mutants (approximately threefold; Fig. 4, G and H; and Video 3). In addition, the frequency of CHE-11::mCherry tracks was also significantly reduced in the retrograde direction (~16% lower in *wdr-60* null cilia; Fig. 4 I).

The IFT-B subunit IFT-74::GFP accumulated at multiple places along cilia in both *wdr-60* mutants (Fig. 4, D and F; Fig. S4 A;

Downloaded from http://rupress.org/jcb/article-pdf/221/1/e202010178/1818538/jcb_202010178.pdf by guest on 10 February 2026

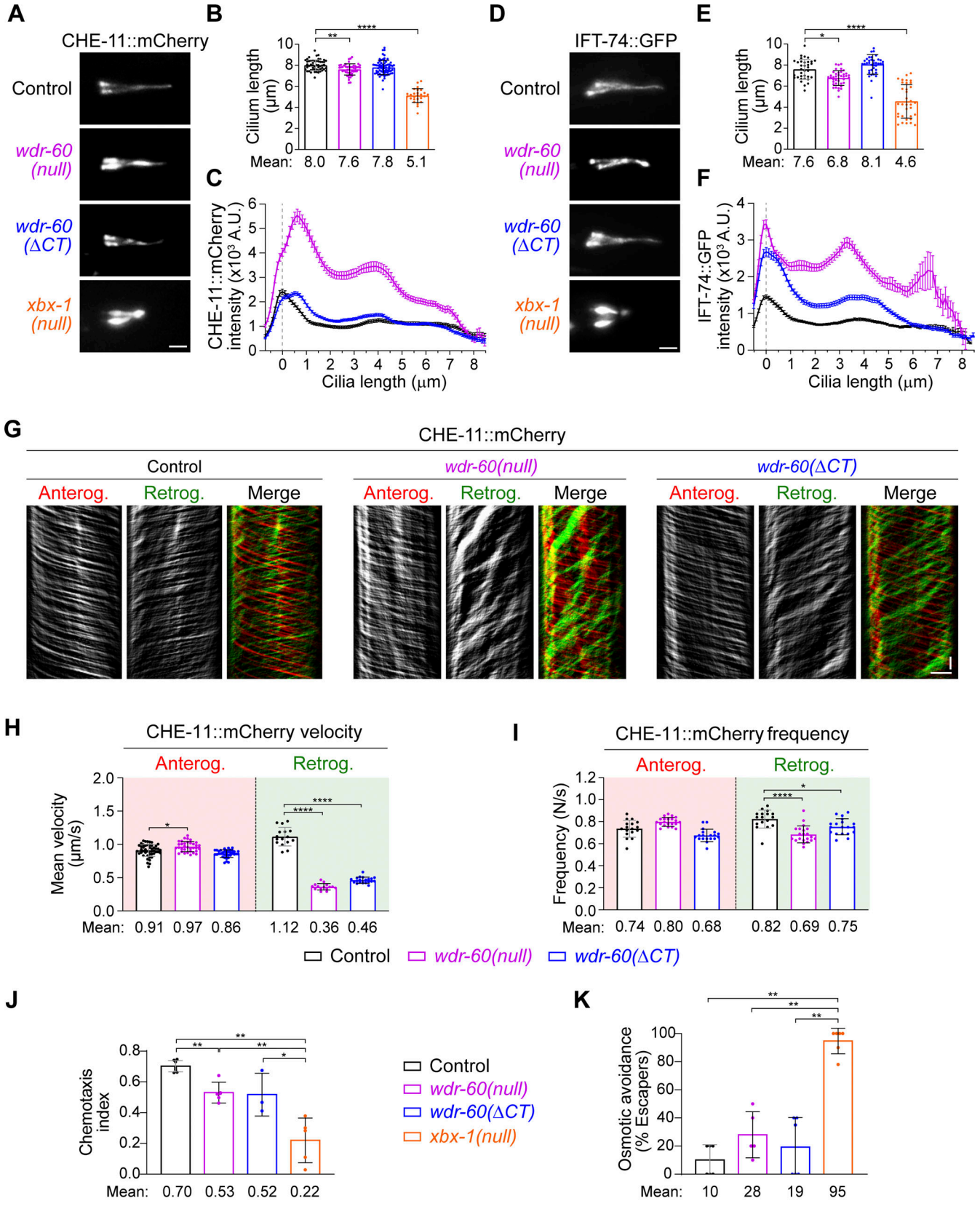

Figure 4. ***wdr-60* mutants have reduced retrograde transport of IFT-A and IFT-B complexes and lower efficiency of cilia-mediated signaling. (A and D)** Phasmid cilia from control, *wdr-60(null)*, *wdr-60(ΔCT)*, and *xbx-1(null)* animals expressing CHE-11::mCherry (A) or IFT-74::GFP (D). **(B and E)** Cilia length measured with CHE-11::mCherry (B) or IFT-74::GFP (E; $n \geq 26$ and $n \geq 34$ cilia, respectively). **(C and F)** Quantification of the average intensity of CHE-11::mCherry (C) and IFT-74::GFP (F) along cilia ($n \geq 42$ and $n \geq 66$ cilia, respectively). **(G)** CHE-11::mCherry kymographs of phasmid cilia from the indicated strains.

Downloaded from http://rupress.org/jcb/article-pdf/221/1/e202010178/1818538/jcb_202010178.pdf by guest on 10 February 2026

(H) Mean velocity of CHE-11::mCherry particles moving on anterograde and retrograde tracks ($n \geq 225$ particle traces were analyzed in ≥15 cilia). **(I)** Frequency of IFT particles detected at the distal segment of cilia ($n \geq 17$ cilia). **(J and K)** WDR-60 is required for efficient sensory cilia functions. **(J)** Chemotaxis index for the attractant IA ($n \geq 450$ animals tracked over ≥3 assays). **(K)** Osmotic avoidance assay to test whether sensory cilia detect a hypertonic glycerol barrier ($n \geq 20$ animals tracked over ≥4 assays). The dynein-2 LIC *xbx-1(null)* strain was used for comparison. XY intensity distribution graph is shown as mean ± SEM, and graphs in columns are shown as mean ± SD. One-way ANOVA followed by Tukey's multiple comparison were used to analyze the datasets in B, H, and I. Kruskal–Wallis test followed by Dunn's multiple comparison were used to analyze the datasets in E. *, $P \leq 0.05$; **, $P \leq 0.01$; ****, $P \leq 0.0001$. Scale bars: 2 µm (A and D); vertical 5 s, horizontal 2 µm (G).

and Video 4), underscoring the importance of WDR-60 in dynein-2–mediated transport of the IFT-B machinery to the ciliary base. When analyzing the distribution of kinesins, we also observed ciliary accumulations for the kinesin-2-associated protein KAP-1 (KIFAP3) and, to a lesser extent, for the distal segment kinesin OSM-3 (KIF17) (Fig. S4, B and C). Altogether, these results show that loss of WDR-60 greatly impairs removal of IFT components from cilia.

To determine the impact of *wdr-60*–associated IFT defects on ciliary functions, we analyzed cilia-dependent behavior in our mutant strains. We tested chemotaxis attraction to isoamyl alcohol (AI) and osmotic tolerance to high concentrations of glycerol (Fig. 4, J and K). Both *wdr-60* mutants showed modest defects in these assays, contrasting with the *xbx-1(null)* mutant, in which chemotaxis attraction and osmotic tolerance is severely compromised. These results suggest that although WDR-60 plays critical roles in dynein-2–mediated IFT, WDR-60–deficient sensory cilia remain partially functional.

TZ integrity and gating function are maintained in *wdr-60* mutants but not in the *xbx-1* mutant

Given that dynein-2 and IFT-A components were recently shown to be required for maintaining the TZ barrier (Jensen et al., 2018; Scheidel and Blacque, 2018; Vuolo et al., 2018), we investigated whether the integrity and gating capacity of the TZ are affected in *wdr-60* and *xbx-1* mutants. We analyzed the localization of four TZ components: TMEM-107, NPHP-4, MKS-6, and MKSR-1 (Jensen et al., 2018; Lambacher et al., 2016; Prevo et al., 2015; Schouteden et al., 2015; Williams et al., 2011). In agreement with what has been reported for CHE-3 and IFT-A mutants (Jensen et al., 2018; Scheidel and Blacque, 2018), we found that loss of XBX-1 results in ectopic localization of these TZ components along the ciliary axoneme (Fig. 5). In contrast, the localization of TZ components in *wdr-60* mutants was indistinguishable from controls (Fig. 5), suggesting that loss of WDR-60 does not affect the integrity of the TZ. To directly test the integrity and gating capacity of the TZ in *wdr-60* mutants, we analyzed its ability to block the entry of RPI-2::GFP (RP2), a component of the periciliary membrane compartment restricted to the base of cilia (Jensen et al., 2018). While loss of XBX-1 resulted in abnormal entry of RPI-2::GFP into cilia, no RPI-2::GFP signal was detectable inside cilia in *wdr-60* mutants (Fig. 5, C and D). These results show that the loss of WDR-60 does not compromise TZ integrity or its gating function in *C. elegans*. In addition, our results uncover an important role for the dynein-2 LIC XBX-1 in maintaining the TZ barrier, likely by stabilizing CHE-3.

WDR-60 is required for dynein-2 passage through the TZ to exit cilia

To more precisely determine where the ciliary pool of dynein-2 accumulates in *wdr-60* mutants, we colabeled GFP::CHE-3 with markers specific for the ciliary base (mCherry::HYLS-1; Schouteden et al., 2015) and for the TZ (MKS-6::mCherry; Williams et al., 2011). In controls, GFP::CHE-3 mainly accumulates at the ciliary base (Fig. 6 A) before entering cilia through the TZ. In contrast, we found that GFP::CHE-3 accumulates mostly at the distal side of the TZ in both *wdr-60* mutants (Fig. 6, B and C).

Recent studies have shown that retrograde trains slow down as they cross the TZ, suggesting that this ciliary gate offers resistance to the passage of retrograde IFT trains (Jensen et al., 2015; Oswald et al., 2018; Prevo et al., 2015). Given that loss of WDR-60 reduces the amount of dynein-2 driving retrograde trains and impairs retrograde IFT velocity (Fig. 3), we hypothesized that WDR-60–deficient retrograde trains may not be able to generate enough force to push through the TZ barrier, and are consequently unable to exit cilia. As removal of MKS-5 (RPGRIP1L), a key component for the assembly of all TZ structures, significantly increases the velocity of IFT trains moving in the TZ region (Jensen et al., 2015), we reasoned that the exit of WDR-60–deficient dynein-2 from cilia might be facilitated by disrupting MKS-5. In agreement, we found that GFP::CHE-3 no longer accumulated on the distal side of the TZ in the *mks-5(tm3100);wdr-60(null)* double mutant (Fig. 7, A–D). Instead, the GFP::CHE-3 distribution profile in this mutant was similar to that observed in controls. This result further supports that retrograde trains driven by dynein-2 are unable to efficiently cross the TZ in *wdr-60* mutants.

To better dissect which TZ modules restrict dynein-2 passage, we next examined GFP::CHE-3 distribution in *wdr-60(null)* cilia after disrupting key components required for the assembly of each TZ module. Removal of the MKS module by inhibiting MKSR-2 (B9D2) or CEP-290 with the *mksr-2(tm2452)* or *cep-290(tm4927)* mutations did not prevent the accumulation of GFP::CHE-3 near the TZ region of *wdr-60(null)* cilia (Fig. 7, E and F; and Fig. S5, A and B). In contrast, disrupting the NPHP module with the *nphp-4(tm925)* mutation in the *wdr-60(null)* background almost completely rescued GFP::CHE-3 accumulation at the distal side of the TZ (Fig. 7, G and H). Joint disruption of NPHP-4 and MKSR-2 further enhanced this rescue effect (Fig. 7, I and J), although we note that both cilia size and GFP::CHE-3 levels along cilia were strongly reduced in the *mksr-2(tm2452);nphp-4(tm925)* double mutant (Fig. 7 K; and Fig. S5, C and D). We conclude that NPHP is the main module restricting the passage of underpowered retrograde trains through the TZ in *wdr-60(null)* cilia.

Next, we tested whether disrupting the TZ could compensate for more severe retrograde IFT defects, such as those caused by a mutation in the microtubule-binding domain of CHE-3 (K2935Q), which completely blocks dynein-2 motility and leads to severely truncated cilia (Yi et al., 2017). In contrast to the

Downloaded from http://rupress.org/jcb/article-pdf/221/1/e202010178/1818538/jcb_202010178.pdf by guest on 10 February 2026

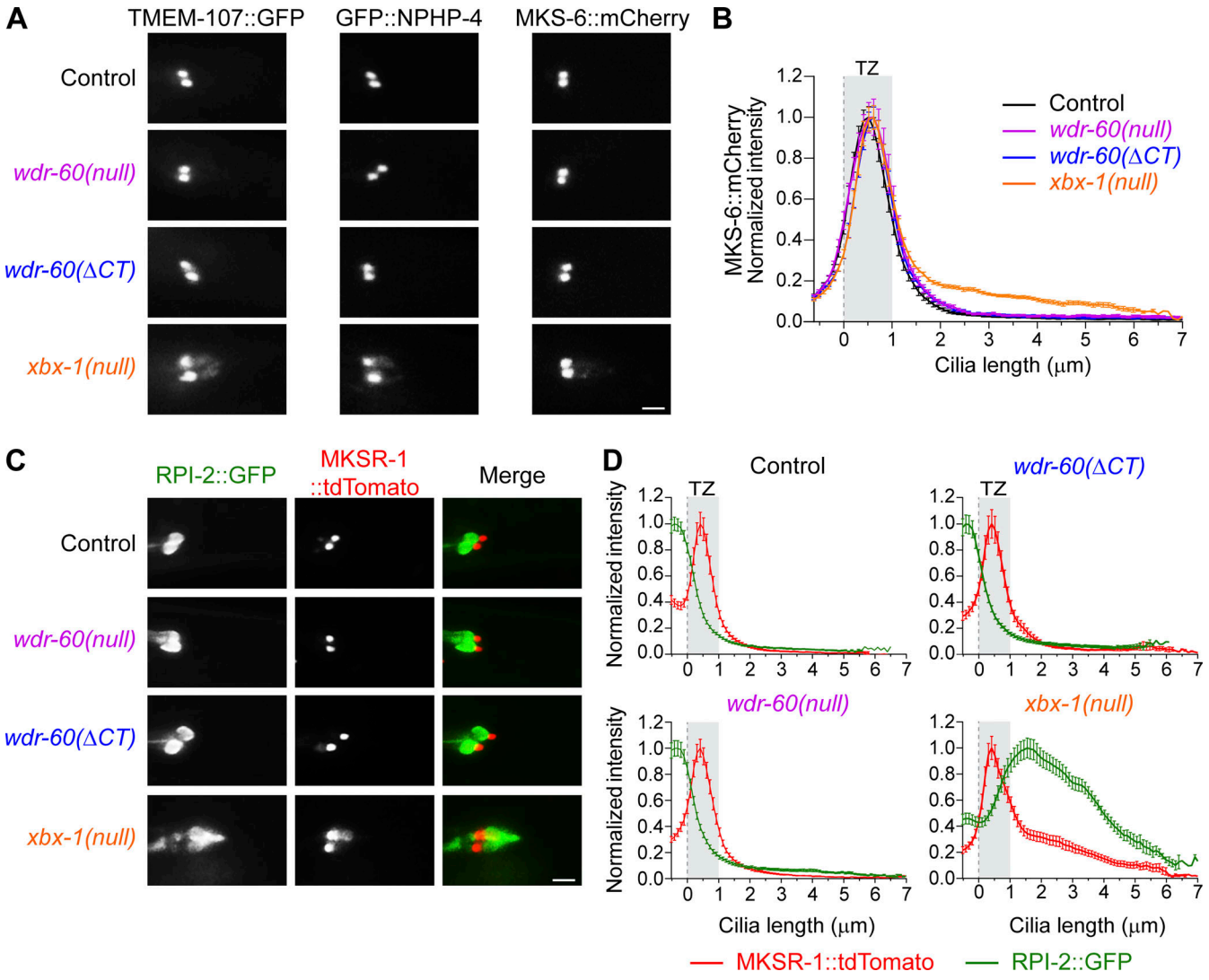

Figure 5. **The integrity and gating function of the TZ are maintained in *wdr-60* mutants but compromised in the *xbx-1* mutant. (A)** Analysis of the localization of several components of the MKS (TMEM-107::GFP and MKS-6::mCherry) and NPHP (GFP::NPHP-4) modules of the TZ in phasmid cilia of the indicated strains. **(B)** Quantification of MKS-6::mCherry signal intensity confined at the TZ and dispersed along cilia ($n \geq 38$ cilia). **(C)** Relative localization of the nonciliary membrane protein RPI-2::GFP to the TZ (labeled with MKSR-1::tdTomato) in phasmid cilia of the indicated strains. **(D)** Signal overlap between these components and quantification of the amount of RPI-2::GFP leaking into cilia ($n \geq 33$ cilia). Gray rectangles highlight the TZ region, defined by MKS-6 and MKSR-1 localization. XY intensity distribution graphs are shown as mean ± SEM. Scale bars: 2 μm.

rescue that we observed earlier in the *wdr-60(null)* mutant background, disrupting MKS-5, NPHP-4, or both MKSR-2/NPHP-4, failed to prevent GFP::CHE-3(K2935Q) accumulation inside cilia (Fig. 8, A–H). These results show that even the complete removal of the TZ barrier is not sufficient to rescue the accumulation of nonmotile dynein-2 inside cilia. Although cilia size slightly increased in the absence of MKS-5 or NPHP-4 (Fig. 8 I), none of the TZ mutants were able to restore anterograde IFT in animals expressing GFP::CHE-3(K2935Q) (Fig. 8 J and Video 5). Thus, IFT requires a minimum amount of functional dynein-2 regardless of the state of the TZ barrier.

The NPHP module restricts dynein-2 movement through the TZ

Next, we investigated whether the kinetics of WDR-60–deficient dynein-2 were altered by the complete removal of the TZ barrier or by the loss of the NPHP module. Consistent with a previous study (Jensen et al., 2015), we observed that loss of MKS-5 increases both the anterograde and retrograde velocities of GFP::CHE-3 particles in the TZ region (Fig. 9, A, C, and D; and Video 6). We also observed a similar, albeit more modest, increase in IFT velocities at the TZ region in the *nphp-4* mutant background. Importantly, we found that loss of either MKS-5 or NPHP-4 increased the retrograde velocity of GFP::CHE-3 in the TZ region of WDR-60–deficient cilia (Fig. 9, A, C, and D; and Video 7). Interestingly, retrograde IFT velocity in the middle segment of *wdr-60(null)* cilia also increased upon the removal of MKS-5 or NPHP-4 (Fig. 9 C), suggesting that clearing the accumulated IFT trains near the TZ allows for more steady buildup of retrograde IFT velocities in these mutants. We note that IFT frequency was not greatly affected by disruption of MKS-5 or NPHP-4 (Fig. 9 B), suggesting that loss of the TZ barrier does not compromise the

Downloaded from http://rupress.org/jcb/article-pdf/221/1/e202010178/1818538/jcb_202010178.pdf by guest on 10 February 2026

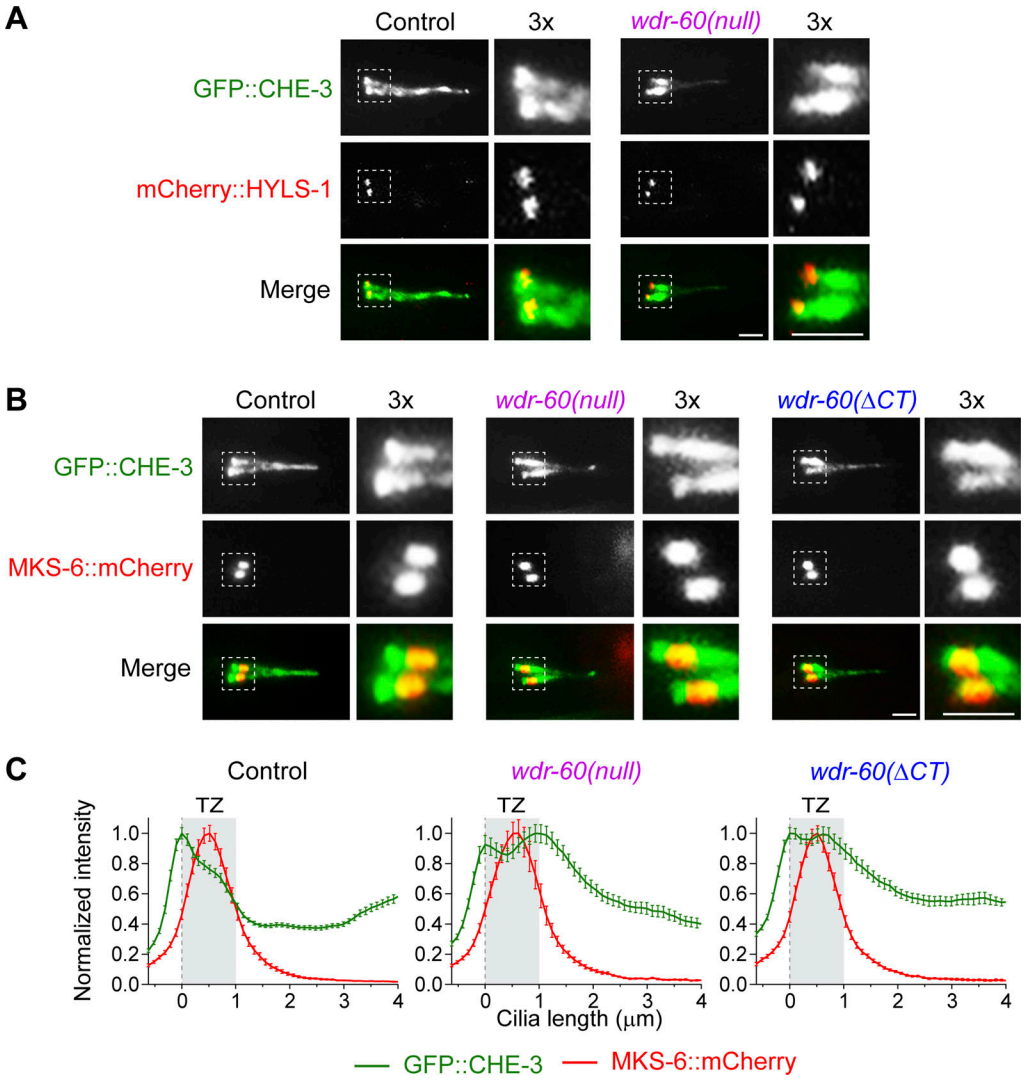

Figure 6. **Dynein-2 accumulates on the distal side of the TZ, unable to complete retrograde IFT in *wdr-60* mutants. (A)** GFP::CHE-3 localization relative to the centriolar wall component mCherry::HYLS-1 at the base of phasmid cilia of the indicated strains. **(B)** GFP::CHE-3 localization relative to the MKS-6::mCherry TZ component in phasmid cilia of the indicated strains. **(C)** Quantification GFP::CHE-3 signal distribution in relation to the TZ, as determined by MKS-6 localization ($n \geq 38$ cilia). Gray rectangles define the TZ region. 3× magnifications of the square section in each micrograph were included to better visualize the distribution of the dynein-2 HC relative to the base and TZ of *wdr-60* mutant cilia. Graphs are shown as mean ± SEM. Scale bars: 2 µm.

poorly understood mechanisms regulating the rate of IFT injection into cilia. Altogether, these results further support that WDR-60 loss impairs dynein-2 passage through the TZ, and that the NPHP module restricts dynein-2 exit from WDR-60–deficient cilia.

Discussion

WDR-60 is incorporated into cilia even in the absence of dynein-2

Our data reveal that WDR-60 is specifically expressed in ciliated sensory neurons in *C. elegans* and undergoes IFT with kinetics similar to those reported for the dynein-2 HC (GFP::CHE-3; Yi et al., 2017). Moreover, our findings indicate that WDR-60(ΔCT) is robustly expressed, showing that the β-propeller is not required for WDR-60 stability. Interestingly, we find that the WDR-60 NT on its own can be recruited to the ciliary base and incorporated into IFT trains, albeit less efficiently than full-length WDR-60. Furthermore, dynein-2 HC destabilization through XBX-1 loss resulted in WDR-60 and WDR-60(ΔCT) sequestration inside cilia, indicating that WDR-60 can enter cilia without dynein-2 but requires its activity in retrograde IFT to exit. Thus, we conclude that the NT of WDR-60 can establish links with other components of the IFT machinery to be incorporated into cilia in the absence of dynein-2. This is in agreement with the weaker but persistent interaction between IFT-B components and the human WDR60[Q631*] truncation lacking the DHC2-binding β-propeller domain (Vuolo et al., 2018).

WDR-60 is required for efficient IFT recycling and contributes to cilia-mediated behavior

Two recent studies in human cells showed that WDR60 loss leads to the misplacement of IFT and signaling particles in cilia

Downloaded from http://rupress.org/jcb/article-pdf/221/1/e202010178/1818538/jcb_202010178.pdf by guest on 10 February 2026

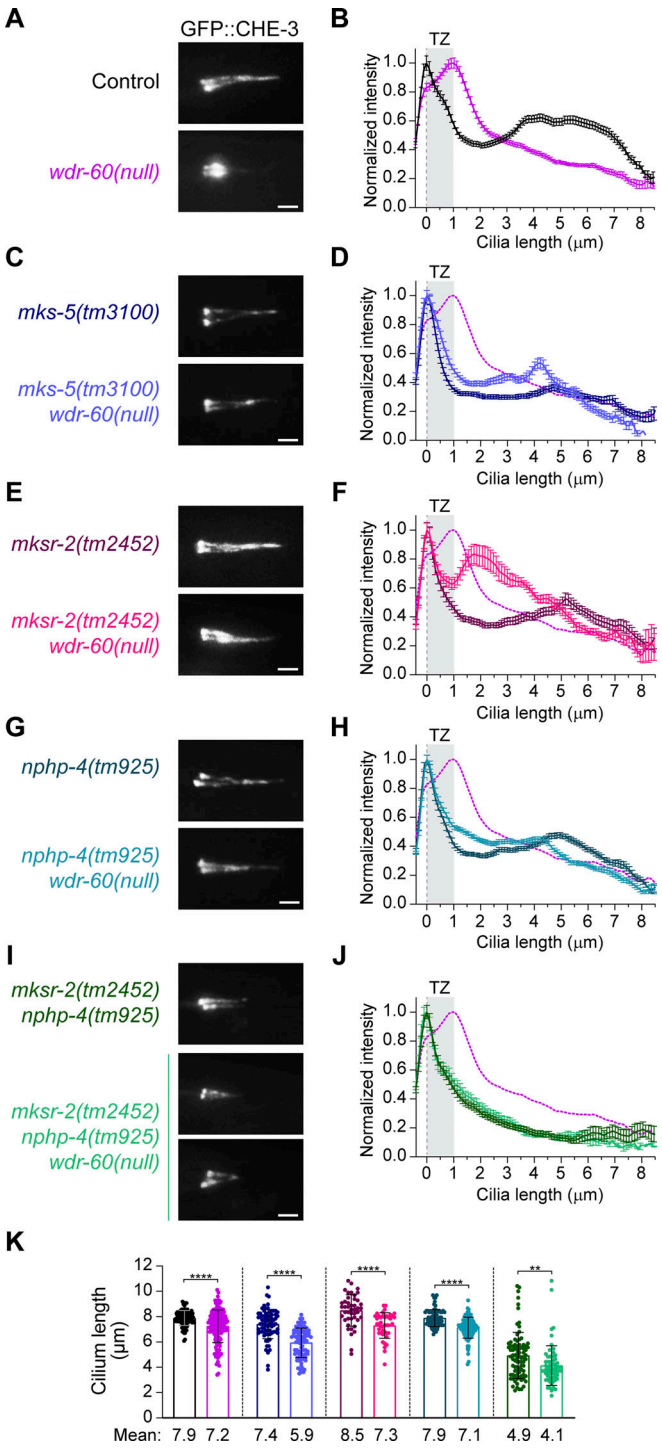

Figure 7. **Disruption of specific TZ components rescues dynein-2 accumulation inside cilia of *wdr-60* mutants. (A, C, E, G, and I)** Representative examples of phasmid cilia of the indicated *wdr-60* and TZ mutant genotypes, expressing GFP::CHE-3. **(B, D, F, H, and J)** Relative distribution of GFP::CHE-3 signal intensity along cilia. The purple dashed line represents the data from the *wdr-60(null)* in B. Gray rectangles highlight the TZ, as previously defined. $n \geq 108$ cilia for B, $n \geq 74$ cilia for D, $n \geq 42$ cilia for F, $n \geq 80$ cilia for H, and $n \geq 64$ cilia for J. XY intensity distribution graphs are shown as mean ± SEM. **(K)** Length of the cilia analyzed in B, D, F, H, and J from the same color-coded genotypes indicated in A, C, E, G, and I. Loss of WDR-60 combined with TZ mutations always resulted in a slight decrease of cilia length relative to the respective TZ mutant control. Graph is shown as mean ± SD. Mann–Whitney *U* test was used to analyze each pair of datasets. **, $P \leq 0.01$; ****, $P \leq 0.0001$. Scale bars: 2 µm.

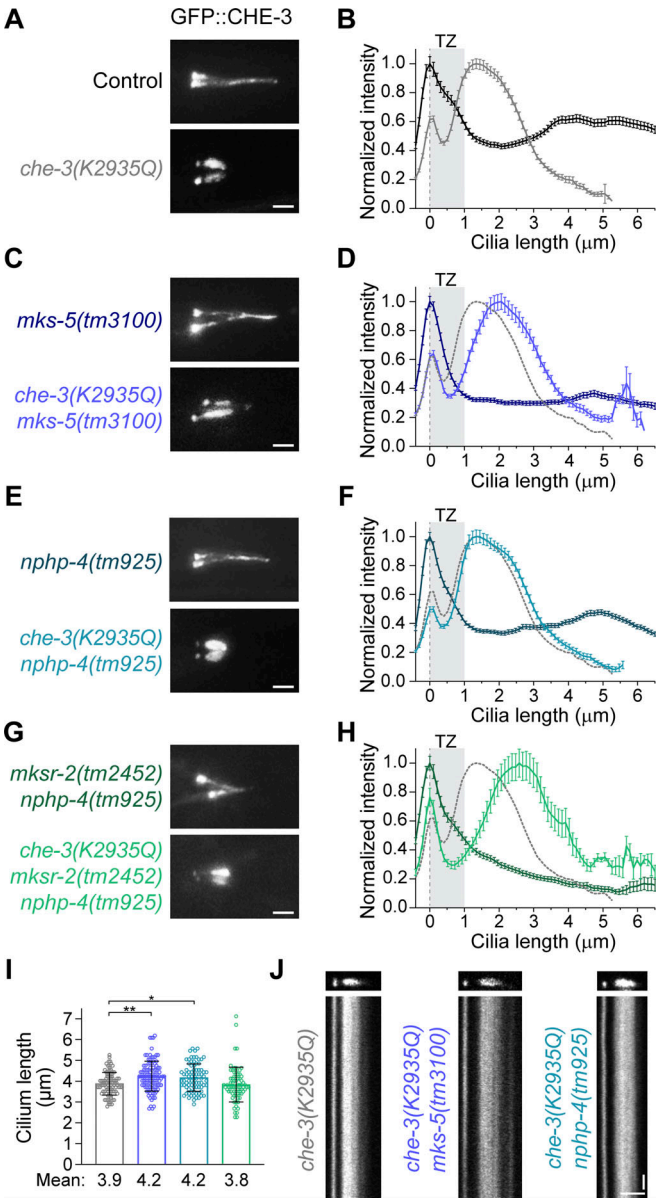

Figure 8. **Complete loss of dynein-2 motility results in ciliary accumulations even when the TZ barrier is completely disrupted. (A, C, E, and G)** Representative examples of phasmid cilia of the indicated TZ mutant genotypes, expressing wild-type GFP::CHE-3 or the nonmotile GFP::CHE-3(K2935Q). **(B, D, F, and H)** Relative distribution of GFP::CHE-3(K2935Q) signal intensity along cilia, in control and TZ mutant backgrounds. The gray dashed line represents the data from the GFP::CHE-3(K2935Q) mutant in B. Gray rectangles highlight the TZ, as previously defined. $n \geq 105$ cilia for B, $n \geq 104$ cilia for D, $n \geq 80$ cilia for F, and $n \geq 86$ cilia for H. XY intensity distribution graphs are shown as mean ± SEM. **(I)** Length of GFP::CHE-3(K2935Q) mutant cilia analyzed in B, D, F, and H, with the same color-coded genotypes as indicated. Graph is shown as mean ± SD. Kruskal–Wallis test followed by Dunn's multiple comparison were used to analyze these datasets. *, $P \leq 0.05$; **, $P \leq 0.01$. **(J)** Cilia and the respective kymographs from the specified strain genotypes. No anterograde or retrograde IFT was detectable in the GFP::CHE-3(K2935Q) mutant, not even in combination with the disruption of MKS-5 or NPHP-4. Scale bars: 2 µm (A, C, E, and G); vertical 5 s, horizontal 2 µm (J).

Downloaded from http://rupress.org/jcb/article-pdf/221/1/e202010178/1818538/jcb_202010178.pdf by guest on 10 February 2026

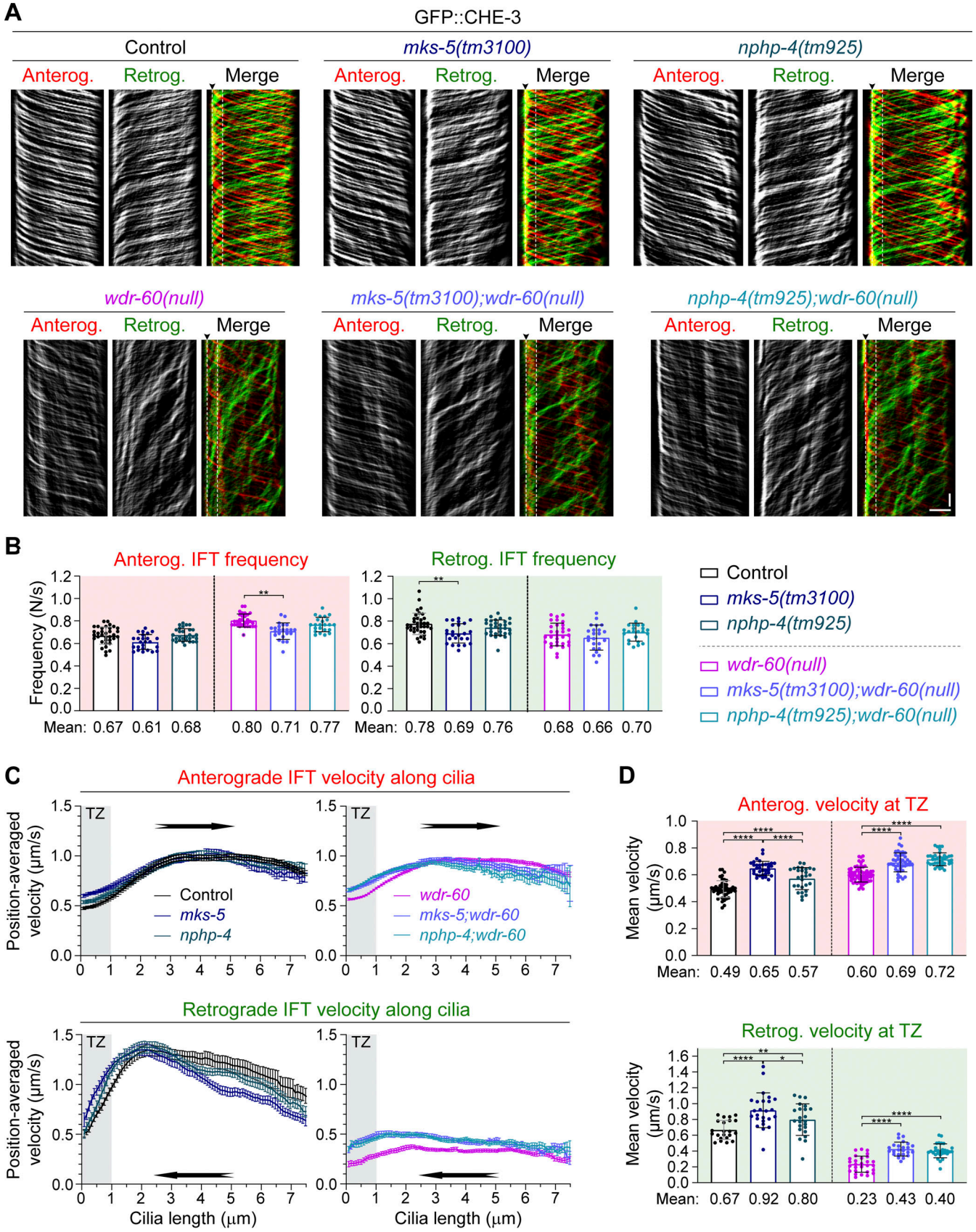

Figure 9. **Disruption of NPHP-4 is sufficient to increase the velocity of WDR-60–deficient dynein-2 through the TZ region. (A)** GFP::CHE-3 kymographs of phasmid cilia from the indicated strains. Single and merge channels for particles moving anterogradely and retrogradely are shown. Arrowhead labels the base, and white dashed line marks the limit of the TZ region (1 µm). Scale bars: vertical 5 s, horizontal 2 µm. **(B)** Frequency of IFT particles detected at the

Downloaded from http://rupress.org/jcb/article-pdf/221/1/e202010178/1818538/jcb_202010178.pdf by guest on 10 February 2026

distal segment of cilia for each represented strain ($n \geq 23$ cilia). **(C)** GFP::CHE-3 velocity moving in the anterograde and retrograde direction along the cilia of the indicated genotypes ($n \geq 345$ particle traces were analyzed in ≥23 cilia for each strain). Gray rectangles highlight the TZ, as previously defined. **(D)** Average velocity of GFP::CHE-3 crossing the TZ region of the same cilia analyzed in C, for each indicated genotype. XY velocity graphs are shown as mean ± SEM, and graphs in columns are shown as mean ± SD. One-way ANOVA followed by Sidak and the Holm–Sidak multiple comparisons were used to analyze the datasets in B and D, respectively. *, $P \leq 0.05$; **, $P \leq 0.01$; ****, $P \leq 0.0001$.

without greatly affecting axoneme extension (Hamada et al., 2018; Vuolo et al., 2018). Remarkably, in spite of the strong defect in retrograde IFT, we show that the *wdr-60(null)* mutant is still capable of building nearly full-length cilia in *C. elegans*, similar to what was observed in WDR60 knockout (KO) human cells (Vuolo et al., 2018). We also show that WDR-60–deficient cilia are at least partially functional in chemotaxis and osmotic tolerance assays, contrasting with the strong behavioral defects exhibited by the *xbx-1(null)* mutant, which assembles severely shortened cilia. The mild chemotaxis and osmotic defects that we observe in *wdr-60* mutants likely mirror the signaling defects underlying *WDR60*-associated SRPS (Cossu et al., 2016; Kakar et al., 2018; McInerney-Leo et al., 2013).

We find that WDR-60 disruption results in accumulation of IFT-74, CHE-11 (IFT140), and the kinesin-2 subunit KAP-1 inside cilia. However, we also show that WDR-60 disruption has different effects on the distribution profile of these IFT components along cilia: IFT-74 (IFT-B) levels peak at the tip and in the middle-to-distal-segment transition (both regions containing microtubule plus ends), while CHE-11 (IFT-A) and KAP-1 levels peak closer to the ciliary base and the TZ region, which is similar to the distribution profile of the dynein-2 motor itself. This suggests that some IFT subunits might be less efficiently incorporated into retrograde IFT trains in WDR-60–deficient cilia. In agreement with this, similar differences in IFT component distribution can be discerned in prior studies using WDR60 KO human cells: IFT88 (IFT-B) accumulates inside their cilia, peaking mostly at the tip, while the peak levels of accumulated IFT140 and IFT43 (both IFT-A) are found closer to the ciliary base (Hamada et al., 2018; Tsurumi et al., 2019; Vuolo et al., 2018).

Interestingly, our results suggest that the WDR-60 NT retains residual activity in IFT, as the accumulation of IFT-A/B particles inside cilia is less pronounced for the *wdr-60(ΔCT)* mutant than for the *wdr-60(null)* mutant. This is consistent with what was observed in WDR60 KO rescue experiments with an equivalent WDR60 β-propeller truncation construct (WDR60 [Q631*]; Vuolo et al., 2018). Apart from the less pronounced IFT accumulations, the loss of the WDR-60 β-propeller leads to defects in dynein-2 incorporation, retrograde IFT kinetics, and cilia-mediated behavior that are similar to those observed upon the complete loss of WDR-60. Thus, our results show that the WDR-60 β-propeller is critical for dynein-2 function.

Normal TZ integrity and gating function in the absence of WDR-60

A recent study uncovered that the dynein-2 HC CHE-3 is necessary for the stability and gating functions of the TZ (Jensen et al., 2018). Consistent with this, we show that loss of the dynein-2 LIC XBX-1 also impairs the integrity and gating functions of the TZ barrier. In a recent study, Vuolo et al. (2018) observed mislocalization of the TZ components TMEM67 and RPGRIP1L (MKS-5 orthologue) in a subset of human RPE1 WDR60 KO cells. In contrast, we do not observe any defects in TZ integrity and gating function in *wdr-60* mutants, as judged by the correct localization of multiple TZ components and the complete RPI-2 exclusion from their sensory cilia. We therefore conclude that the integrity and function of the TZ barrier are maintained in the absence of WDR-60 in *C. elegans*. The difference in TZ susceptibility to WDR60 loss may arise from the variations in TZ structure observed between different types of cilia (Akella et al., 2019; Jana et al., 2018) or from potential differences in the minimal threshold of dynein-2 function required for maintaining TZ integrity in each model system.

Disruption of WDR-60 reduces dynein-2 loading into cilia and the kinetics of retrograde IFT

Prior studies reported that WDR60 loss resulted in the complete disappearance of dynein-2 LIC from the base and axoneme of cilia (Hamada et al., 2018; Vuolo et al., 2018), but no detectable difference was observed in the recruitment of the dynein-2 HC to the ciliary base (Vuolo et al., 2018). Our analyses of endogenously labeled dynein-2 HC and LIC in *C. elegans* reveals that both subunits still colocalize inside WDR-60–deficient cilia. Importantly, the efficiency of dynein-2 HC recruitment to cilia is substantially decreased in the absence of WDR-60 or its dynein-2–binding β-propeller domain. Given that dynein-2 HC levels in the soma of ciliated sensory neurons are not greatly altered by the loss of WDR-60, our results argue that WDR-60 directly contributes to dynein-2 recruitment to cilia rather than having a significant role in dynein-2 HC stabilization, as is the case for dynein-2 LIC (Taylor et al., 2015; Toropova et al., 2019).

A recent structural study revealed that binding of the WDR60-WDR34 heterodimer contributes to the asymmetric conformation of the autoinhibited dynein-2 complex, and this was proposed to facilitate dynein-2 incorporation onto anterograde IFT trains (Toropova et al., 2017; Toropova et al., 2019). Our quantifications of dynein-2 HC (GFP::CHE-3) signal on anterograde tracks inside *wdr-60* mutant cilia provide the first direct evidence for this model in vivo. This conclusion is supported by the observation that the reduction in dynein-2 loading onto anterograde trains (approximately threefold) is even greater than the reduction in dynein-2 recruitment to cilia (approximately twofold) in *wdr-60* mutants.

Intriguingly, the observation that a fraction of dynein-2 motors still become incorporated onto anterograde IFT trains indicates that WDR-60 is not the only link that dynein-2 can establish with anterograde trains. This conclusion is further supported by the recent report of a direct interaction between dynein-2 LIC and IFT54 of the IFT-B complex (Zhu et al., 2021)

Downloaded from http://rupress.org/jcb/article-pdf/221/1/e202010178/1818538/jcb_202010178.pdf by guest on 10 February 2026

and by cryo-EM data suggesting that the main contacts between anterograde IFT trains and dynein-2 motors may also involve the HC (Toropova et al., 2019).

Although less dynein-2 reaches the cilium tip to then power retrograde IFT, we find that the frequency of retrograde IFT is only mildly affected in the absence of WDR-60. Taken together with the observation that dynein-2 does not accumulate at the ciliary tip, this result argues that WDR-60 is dispensable for dynein-2 activation and the start of retrograde IFT.

Underpowered retrograde IFT trains fail to push through the TZ barrier to exit cilia in *wdr-60* mutants

Emerging evidence points to an important interplay between IFT-A and the BBSome in regulating the traffic of G protein–coupled receptors in and out of cilia across the TZ, in part by coupling the receptors to IFT trains (reviewed in Nachury and Mick, 2019). As a dense gating structure, the TZ has been shown to slow down the passage of motor-powered IFT trains, supporting the notion that this physical barrier offers substantial resistance to the passage of IFT trains (Jensen et al., 2015; Oswald et al., 2018; Prevo et al., 2015). However, little is known about the mechanisms that enable the IFT machinery to pass through the TZ barrier.

Our live imaging analysis shows that WDR-60–deficient retrograde IFT trains are driven by fewer dynein-2 motors, at severely reduced velocity, and accumulate at the distal side of the TZ. We propose that the accumulation of these underpowered IFT trains reflects their inability to push through the TZ barrier (Fig. 10). Additional lines of evidence support a model in which a force production threshold needs to be met for retrograde IFT to cross the TZ barrier: (a) in experiments using purified "untrapped" dimers of GST-dynein-2 motor domains, maximum microtubule gliding velocity can be achieved only after a certain dynein-2 concentration is reached (Toropova et al., 2017); (b) the same study showed that DNA origamis mimicking IFT trains were transported less efficiently (less processive runs) when attached to three untrapped dynein-2 motor dimers than when attached to seven dimers (Toropova et al., 2017); (c) the cooperative action of multiple dynein-2 motors in retrograde IFT has been shown to be capable of generating considerable forces (≥25 pN) to move against resisting loads (Roberts, 2018; Shih et al., 2013); and (d) we show in this study that removing the resistance offered by the TZ rescues the exit of the underpowered retrograde IFT trains driven by fewer dynein-2 motors in *wdr-60* mutants.

Our findings are also consistent with the "motorized plough" model, which posits that dynein-2 motors remove IFT trains and their cargoes out of the cilium by dragging them while pushing through the TZ barrier (Nachury and Mick, 2019). We note, nonetheless, that we cannot fully exclude the possibility that WDR-60 might also contribute in other ways to retrograde IFT or ciliary exit.

The NPHP module offers resistance to dynein-2 passage through the TZ

Our results reveal that disrupting MKS-5, the most upstream TZ assembly factor, can rescue the exit of underpowered retrograde IFT trains from *wdr-60(null)* cilia. We then dissected which TZ modules offer resistance to dynein-2 exit by targeting their respective upstream components. We find that removal of the NPHP module by disrupting NPHP-4 almost completely rescues the exit of WDR-60–deficient dynein-2 from cilia, while the loss of the MKS module by disrupting MKSR-2 or CEP-290 did not. Given that previous studies showed that the recruitment of NPHP-4 and the assembly of the NPHP module are unaffected by the loss of either CEP-290 or MKSR-2 (Blacque and Sanders, 2014; Li et al., 2016; Schouteden et al., 2015), our findings support a pivotal role for the NPHP module in restricting dynein-2 passage through the TZ. Interestingly, in addition to disrupting the assembly of the NPHP module, NPHP-4 loss has also been shown to reduce the number of Y-links and their densities (Jensen et al., 2015; Lambacher et al., 2016). However, additional experimental work will be required to directly determine whether Y-links themselves influence the passage of IFT trains through the TZ.

Consistent with an important role for NPHP-4 and the NPHP module in restricting dynein-2 crossing of the TZ, studies in *C. elegans* and *Chlamydomonas* have shown that NPHP4 loss weakens and permeabilizes the TZ barrier, allowing entry of normally excluded cytoplasmic proteins and reducing the retention of ciliary proteins (Awata et al., 2014; Jauregui et al., 2008; Williams et al., 2011). In agreement with this, we find that removal of NPHP-4 increases the velocity of both anterograde and retrograde IFT trains crossing the TZ roadblock, particularly improving the retrograde velocity of underpowered WDR-60–deficient trains exiting cilia. This effect was even comparable with the increased IFT velocity in the TZ region that results from the disruption of MKS-5 in *wdr-60(null)* cilia. This supports the idea that even though NPHP-4 loss does not impair the TZ to the same extent as MKS-5 inhibition, it considerably reduces the resistance offered to IFT trains crossing the TZ barrier.

Interestingly, our results also indicate that even the complete removal of the TZ barrier is not sufficient for clearing out nonmotile CHE-3(K2935Q) dynein-2 from cilia. This finding implies that, although reduced, dynein-2 motors powering WDR-60–deficient retrograde IFT trains make an important contribution to the rescue observed upon disruption of the TZ barrier.

Taken together, our results provide direct evidence that the NPHP module of the TZ offers resistance to the passage of dynein-2–driven IFT trains and strongly support that dynein-2 motors need to reach a minimal force-generating threshold to power passage of retrograde trains through the TZ barrier to exit cilia.

Materials and methods

C. elegans maintenance and strain generation

C. elegans strains were maintained at 20°C on standard nematode growth medium (NGM) plates seeded with *Escherichia coli* OP50 bacteria and crossed using standard procedures (Brenner, 1974). Hermaphrodite worms were used in all assays. Mutant genotyping was performed by standard PCR. The *wdr-60* locus was

Downloaded from http://rupress.org/jcb/article-pdf/221/1/e202010178/1818538/jcb_202010178.pdf by guest on 10 February 2026

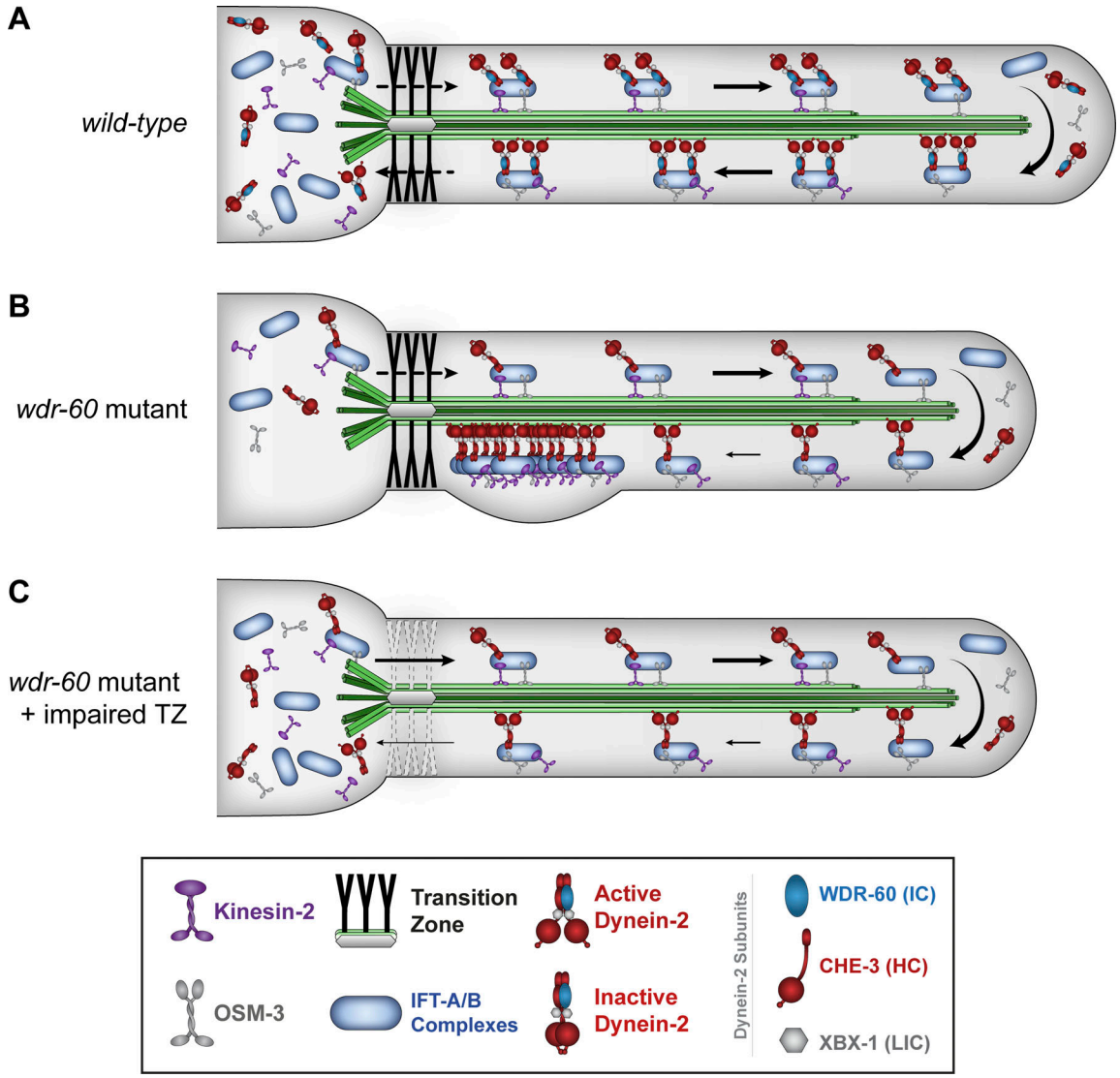

Figure 10. **Model for how WDR-60 contributes to efficient dynein-2–mediated retrograde IFT, and the crossing of the TZ to recycle the IFT machinery. (A)** In wild-type *C. elegans* cilia, kinesin motors carry dynein-2 as a cargo on anterograde IFT trains across the TZ to enter the cilium compartment and reach the ciliary tip. After rearrangement, dynein-2 transports trains in the retrograde direction, crossing the TZ barrier to return them to the base of the cilium, so they can be recycled. **(B)** In the absence of WDR-60, less dynein-2 is recruited and loaded onto anterograde IFT trains to be incorporated into cilia. Consequently, fewer dynein-2 motors are available at the ciliary tip to power the newly rearranged retrograde trains. These underpowered dynein-2–driven trains move at slower velocities and tend to accumulate at the distal side of the TZ, unable to generate enough force to cross this barrier. **(C)** Disrupting the NPHP module reduces the resistance offered by the TZ to the passage of IFT trains, facilitating the exit of retrograde IFT to the cilium base and compensating for the less efficient WDR-60–deficient dynein-2 trains.

engineered by CRISPR-Cas9 using germline microinjection of Cas9 and specific gRNA-expressing (5′-GACAAACGCAATTCGCAGA-3′ and 5′-TGTTCTAGAAGATCCCGCG-3′) constructs, supplemented with homology templates consisting in DNA oligonucleotides or large DNA fragments partially single stranded (Dokshin et al., 2018). The presence of the desired alleles was confirmed by PCR-based genotyping. New strains were outcrossed four to six times to ensure the absence of potential CRISPR-Cas9 off-target mutations. *C. elegans* strains and primers used in this study are listed in Table S2 and Table S3, respectively.

Fluorescence imaging

All imaging was performed using young adult hermaphrodite worms, with the exception of the aging experiments, in which animals at larval stage 2 and 7/18 days after adulthood were also imaged for comparison. All animals used for imaging were immobilized using 5–10 mM levamisole and were placed on a 5% agarose pad mounted on a microscope slide.

Cilia imaging to generate signal-intensity distribution profiles was performed using an Axio Observer microscope (Zeiss) equipped with a Plan-Apochromat 63×/1.46 NA oil objective lens and an Orca Flash 4.0 camera (Hamamatsu) and controlled by Zen software (Zeiss). Z-stacks were acquired with 0.4 µm between each z-section.

Time-lapse imaging of IFT was performed using an Olympus IX81 inverted microscope coupled to an Andor Revolution XD spinning disk confocal system composed of an iXon^{EM}+ DU-897 with 2× port coupler camera (Andor Technology), a solid-state

Downloaded from http://rupress.org/jcb/article-pdf/221/1/e202010178/1818538/jcb_202010178.pdf by guest on 10 February 2026

laser combiner (ALC-UVP 350i; Andor Technology), and a CSU-X1 confocal scanner (Yokogawa Electric Corp.), controlled by Andor IQ3 software (Andor Technology). 200 frames were recorded for each phasmid cilium at 3 frames/s (333 ms per frame) using an UPLSAPO 100×/1.40 NA oil objective lens. All imaging was performed in temperature-controlled rooms kept at 20°C.

Image processing and analyses of live IFT

Z-stack and time-lapse series were processed and analyzed with Fiji software (ImageJ v2.0.0-rc-56/1.52 p). Fluorescence signal of ciliary components (such as IFT-74::GFP, CHE-11::mCherry, and GFP::CHE-3) were used to measure the length of cilia in wild-type and mutant strains from the center of the base to the ciliary tip. The profile of IFT particle distribution was determined along cilia using fluorescently labeled IFT markers. The signal intensity of each pixel was measured from the base to the tip of each cilium, and the relative signal distribution of particles was determined. When indicated, signal intensity values of each profile were normalized to their point of maximum intensity to facilitate comparison between profiles from different mutant combinations, and in these instances the total signal from base to tip was also determined and plotted separately.

Kymographs were generated in ImageJ (National Institutes of Health) using the KymographClear toolset plugin (v2.0; Mangeol et al., 2016). To ensure the quality of the data used to analyze IFT dynamics, only cilia without severe malformations and completely visible in single stable focal planes were used to generate kymographs. KymographDirect software (v2.1; Mangeol et al., 2016) was used to analyze IFT dynamics, which takes into account background and bleaching automatically and is able to distinguish and separate anterograde from retrograde IFT. Anterograde tracks of individual IFT particles along the whole cilium length were automatically detected by the program as done in Mijalkovic et al. (2017) and validated. Given the severity of the retrograde IFT phenotypes in *wdr-60* mutants, the program was unable to robustly detect the retrograde tracks of IFT particles. To account for that, all retrograde tracks (both in mutants and in controls) had to be drawn manually. Continuous IFT tracks drawn in the prior step were then used to automatically determine IFT velocities at different positions along cilia with KymographDirect. When average velocities were calculated for particular subregions of the axoneme, they were subgrouped as follows: TZ (0–1 µm), middle segment (1–4.5 µm), and distal segment (4.5 µm to ciliary tip).

To determine the frequency of anterograde and retrograde IFT events (data in Figs. 1 G, 3 F, 4 I, and 9 B), we employed the approach used in Mijalkovic et al. (2017). A vertical straight line was drawn to cross the same position at the ciliary distal segment of each anterograde or retrograde kymograph. The line drawn on each kymograph was then used to generate an intensity profile plot, which allowed to score the number of IFT events in either direction by counting the number of intensity spikes. This quantification reflects the number of distinguishable GFP::CHE-3 particles that move in either direction over time.

The average signal intensities of anterogradely or retrogradely moving GFP::CHE-3 particles were determined using KymographDirect as in Mijalkovic et al. (2017). The software automatically measured the intensity of all pixels composing each IFT track, including the retrograde tracks that had to be drawn manually, as mentioned above. The pixel values were then averaged to provide a single intensity value, representative of each individual track. Each point of GFP::CHE-3 intensity plotted in Fig. 3 G corresponds to the average of all of the tracks (a minimum of 15) from a single cilium, for either anterograde or retrograde IFT. At least 15 cilia were used per strain to determine the average GFP::CHE-3 intensity particles moving in either direction.

Dye filling

A stock solution containing 8 mg/ml of DiI (1,1′-dioctadecyl-3,3,3′,3′-tetramethylindocarbocyanine perchlorate) in dimethyl formamide was prepared in advance and stored at −20°C. One confluent but not starved plate of worms from the strain to be tested was grown for each experiment, and a fresh dilution of DiI solution at 2.5 µg/ml was prepared in M9 (86 mM NaCl, 42 mM Na_2HPO_4, 22 mM KH_2PO_4, and 1 mM $MgSO_4$) and kept in the dark covered with aluminum foil. Worms were collected and washed in M9 and incubated in 500 µl of working DiI solution for 1 h at room temperature in the dark, with occasional flipping of the tubes. After washing in M9, worms were placed on an NGM seeded plate for 3 h at 20°C to further reduce the background of ingested dye. The neuronal uptake of dye was then examined using the Axio Observer microscope as described above. At least 20 adult hermaphrodite worms were examined for each strain in ≥2 independent experiments.

Chemosensing assays

Chemotaxis to IA, an attractant compound, was assessed using 150–200 well-fed synchronized adult worms grown at 20°C per assay, following the guidelines of Bargmann et al. (1993). Briefly, worms were washed three times in CTX buffer (1 mM $CaCl_2$, 1 mM $MgSO_4$, and 5 mM KH_2PO_4, pH 6.0) and placed on a 10-cm CTX plate without bacteria, at the starting/origin point. This origin point was set to be at the edge of the plate, equidistant to 10% IA attractant (in absolute ethanol) and vehicle (absolute ethanol) regions, which were drawn at opposite ends of the plate. Before adding 10 µl of 10% IA to the attractant site and 10 µl of 100% ethanol (solvent) to the control site, a solution of 1 M sodium azide (NaN_3) was added to these two points. The sodium azide serves to immobilize any worms that reach the attractant or vehicle (control) regions, preventing them from moving away. After being placed at the origin point, worms were allowed to freely explore the plate for 1 h at 20°C, after which their localization and chemotaxis index was determined. The chemotaxis index can vary from 1.0 to −1.0 and was calculated as follows: Chemotaxis index = (number of worms at the attractant site − number of worms at the control site) / total number of worms.

Osmotic avoidance assay

Osmotic avoidance assays were performed on NGM nonseeded plates at room temperature (~20°C), following the guidelines of Sanders et al. (2015). Each repeat was performed using five

Downloaded from http://rupress.org/jcb/article-pdf/221/1/e202010178/1818538/jcb_202010178.pdf by guest on 10 February 2026

young adult hermaphrodite worms of each strain isolated before the experiment. Worms were placed inside a glycerol ring with a diameter of ∼1 cm, freshly prepared with a tube dipped in a 59% glycerol solution. Worm behavior was immediately monitored for 10 min to determine whether they avoided crossing the glycerol ring. Worms that left the ring or stayed in contact with its glycerol border for >20 s were classified as escapers. Wild-type and *xbx-1(null)* worms were used as controls.

Immunoblotting

For immunoblots of *C. elegans* extracts, four plates of hermaphrodites reaching confluence were collected and washed three times in M9, and the worm pellet was resuspended in an equal volume of 4× SDS-PAGE sample buffer (250 mM Tris-HCl, pH 6.8, 30% [vol/vol] glycerol, 8% [wt/vol] SDS, 200 mM DTT, and 0.04% [wt/vol] bromophenol blue). The worm suspension in sample buffer was supplemented with ∼20 µl of glass beads, incubated for 5 min at 95°C, and vortexed for an additional 5 min. After boiling and vortexing twice, samples were centrifuged at 20,000 *g* for 1 min at room temperature, and supernatants were collected. 20% of each sample was loaded and resolved on a 10% SDS-PAGE gel and transferred to 0.2-µm nitrocellulose membranes (GE Healthcare). Membranes were rinsed in PBS (137 mM NaCl, 2.7 mM KCl, 8.1 mM Na_2HPO_4, and 1.47 mM KH_2PO_4) supplemented with 0.1% Tween-20 (PBS-T, pH 7.4), and then blocked with 5% (wt/vol) nonfat dry milk in PBS-T for 1 h. Subsequently, membranes were incubated with mouse anti-FLAG M2 antibody (1:500; Sigma-Aldrich) or mouse anti-α-tubulin B512 antibody (1:5,000; Sigma-Aldrich) overnight at 4°C. On the following day, membranes were washed three times in PBS-T for 10 min each. Membranes were then incubated with secondary antibodies coupled to HRP (1:10,000; Jackson ImmunoResearch) for 1 h at room temperature and washed three times in PBS-T for 5 min each. Pierce ECL Western Blotting Substrate (Thermo Fisher Scientific) was added to membranes to visualize proteins by chemiluminescence using x-ray film or a Chemidoc station (Bio-Rad). Each immunoblot was repeated several times using samples from independent experiments. The predicted protein sizes were based on the NCBI WDR-60 sequence (NP_001367569.1).

Data analyses and statistics

Statistical analyses of datasets were performed using GraphPad Prism software (v8). For the majority of the experiments, ≥20 worms from different plates were examined for each strain, in at least three independent experiments. Shapiro–Wilk and Kolmogorov–Smirnov normality tests were performed to determine whether sample groups followed Gaussian distributions, which dictated the choice between the use of parametric or nonparametric statistical tests. One-way ANOVA, followed by comparison of the mean of each experimental group with the mean of the control group, was used to analyze parametric datasets; otherwise, we used the nonparametric Kruskal–Wallis test. Follow-up multiple comparison tests were selected according to GraphPad Prism software suggestions. For single-comparison statistical analyses of parametric datasets, the two-tailed Student's *t* test was used, while the two-tailed Mann–Whitney *U* test was used for nonparametric data. Differences were considered significant at P values <5% (*, P ≤ 0.05; **, P ≤ 0.01; ***, P ≤ 0.001; and ****, P ≤ 0.0001). XY velocity and intensity distribution graphs are shown as mean ± SEM. Graphs in columns are shown as mean ± SD.

Online supplemental material

Fig. S1 shows a schematic of the *C27F2.1* locus organization in the *C. elegans* genome and the strategies used to generate *wdr-60* mutants and the 3xFLAG::GFP knock-in. Fig. S2 shows that WDR-60::3xFLAG::GFP expression is restricted to ciliated sensory neurons; it also shows the average GFP::CHE-3 intensity in soma of phasmid sensory neurons of control and *wdr-60* mutants. Fig. S3 shows the analyses of WDR-60–associated phenotypes at different stages of development and aging. Fig. S4 shows kymographs illustrating IFT-74::GFP kinetics in *wdr-60* mutants and the ciliary distribution profile for KAP-1 and OSM-3. Fig. S5 shows the levels of ciliary GFP::CHE-3 in the mutant backgrounds of *wdr-60* and disrupted TZ components, and that the GFP::CHE-3 accumulation at the distal side of the TZ associated with WDR-60 loss is not ameliorated in the *cep-290(tm4927)* mutant background. Table S1 contains the nomenclature of *C. elegans* proteins that are mentioned in the text, and their corresponding homologues or orthologues in humans. Table S2 contains the list of strains used in this study. Table S3 contains the list of primers used in this study. Video 1 shows GFP::CHE-3 and WDR-60::GFP undergoing IFT in *C. elegans* phasmid cilia. Video 2 shows the dynamics of GFP::CHE-3 in *C. elegans* phasmid cilia from control and *wdr-60* mutants. Video 3 shows the dynamics of CHE-11::mCherry in *C. elegans* phasmid cilia from control and *wdr-60* mutants. Video 4 shows the dynamics of IFT-74::GFP in *C. elegans* phasmid cilia from control and *wdr-60* mutants. Video 5 shows the dynamics of GFP::CHE-3(K2935Q) in *C. elegans* phasmid cilia from control, *mks-5(tm3100)*, and *nphp-4(tm925)* strains. Video 6 shows the dynamics of GFP::CHE-3 in *C. elegans* phasmid cilia from control, *mks-5(tm3100)*, and *nphp-4(tm925)* strains. Video 7 shows the dynamics of GFP::CHE-3 in *C. elegans* phasmid cilia from *wdr-60(null)*, *wdr-60(null);mks-5(tm3100)*, and *wdr-60(null);nphp-4(tm925)* mutants.

Acknowledgments

We thank Dr. Alexander Dammermann (University of Vienna, Vienna, Austria) for discussions and members of the Dantas lab for critical reading of the manuscript. The authors also thank Drs. Alexander Dammermann (University of Vienna, Vienna, Austria), Erwin Peterman (Vrije Universiteit Amsterdam, Amsterdam, Netherlands), Guangshuo Ou (Tsinghua University, Beijing, China), Oliver Blacque (University College Dublin, Dublin, Ireland), Michel Leroux (Simon Fraser University, Burnaby, Canada), and Bram Prevo (University of Edinburgh, Edinburgh, Scotland) for providing *C. elegans* strains.

This work was financed by Fundo Europeu de Desenvolvimento Regional (FEDER) through the COMPETE 2020 Operacional Programme for Competitiveness and Internationalisation (POCI), Portugal 2020, and Portuguese funds through Fundação para a Ciência e a Tecnologia (FCT)/Ministério da Ciência, Tecnologia e Ensino Superior in the framework of the project POCI-01-0145-FEDER-029471 (PTDC/BIA-BID/29471/2017) to T.J. Dantas.

Downloaded from http://rupress.org/jcb/article-pdf/221/1/e202010178/1818538/jcb_202010178.pdf by guest on 10 February 2026

A.X. Carvalho, R. Gassmann, C.M.C. Abreu, and T.J. Dantas were supported by the FCT: CEECIND/01967/2017, CEECIND/00333/2017, CEECIND/01985/2018, and CEECIND/00771/2017, respectively. N. Vieira is a Junior Researcher under the scope of the FCT Transitional Rule DL57/2016, and her work was supported by a 2016 NARSAD Young Investigator Grant (#24929) from the Brain and Behavior Research Foundation. D.R.M. Rodrigues received a PhD fellowship from FCT (SFRH/BD/143985/2019) and support from the Biomedical Sciences PhD program at Instituto de Ciências Biomédicas Abel Salazar (ICBAS). Some strains were provided by the National Bioresource Project for *C. elegans* and by the Caenorhabditis Genetics Center (CGC), which is funded by the National Institutes of Health Office of Research Infrastructure Programs (P40 OD010440).

The authors declare no competing financial interests.

Author contributions: A.R.G. De-Castro and D.R.M. Rodrigues performed most of the experiments, actively contributed to the experimental design, analyzed data, and helped prepare figures and write the manuscript. M.J.G. De-Castro helped with several experiments, quantifications, and figure preparation. N. Vieira carried out the chemotaxis assay, and C. Vieira generated some strains. R. Gassmann and A.X. Carvalho provided strains, reagents, and equipment and helped with experimental design. T.J. Dantas and C.M.C. Abreu conceived the project, designed and helped with experiments, analyzed and interpreted data, prepared figures, wrote the manuscript, and supervised the project. All authors read the manuscript and provided input for the final version.

Submitted: 31 October 2020
Revised: 20 September 2021
Accepted: 13 October 2021

References

Akella, J.S., M. Silva, N.S. Morsci, K.C. Nguyen, W.J. Rice, D.H. Hall, and M.M. Barr. 2019. Cell type-specific structural plasticity of the ciliary transition zone in C. elegans. *Biol. Cell.* 111:95–107. https://doi.org/10.1111/boc.201800042

Asante, D., N.L. Stevenson, and D.J. Stephens. 2014. Subunit composition of the human cytoplasmic dynein-2 complex. *J. Cell Sci.* 127:4774–4787. https://doi.org/10.1242/jcs.159038

Awata, J., S. Takada, C. Standley, K.F. Lechtreck, K.D. Bellvé, G.J. Pazour, K.E. Fogarty, and G.B. Witman. 2014. NPHP4 controls ciliary trafficking of membrane proteins and large soluble proteins at the transition zone. *J. Cell Sci.* 127:4714–4727. https://doi.org/10.1242/jcs.155275

Bae, Y.K., and M.M. Barr. 2008. Sensory roles of neuronal cilia: cilia development, morphogenesis, and function in C. elegans. *Front. Biosci.* 13:5959–5974. https://doi.org/10.2741/3129

Bargmann, C.I., E. Hartwieg, and H.R. Horvitz. 1993. Odorant-selective genes and neurons mediate olfaction in C. elegans. *Cell.* 74:515–527. https://doi.org/10.1016/0092-8674(93)80053-H

Blacque, O.E., and A.A. Sanders. 2014. Compartments within a compartment: what C. elegans can tell us about ciliary subdomain composition, biogenesis, function, and disease. *Organogenesis.* 10:126–137. https://doi.org/10.4161/org.28830

Blacque, O.E., E.A. Perens, K.A. Boroevich, P.N. Inglis, C. Li, A. Warner, J. Khattra, R.A. Holt, G. Ou, A.K. Mah, et al. 2005. Functional genomics of the cilium, a sensory organelle. *Curr. Biol.* 15:935–941. https://doi.org/10.1016/j.cub.2005.04.059

Blisnick, T., J. Buisson, S. Absalon, A. Marie, N. Cayet, and P. Bastin. 2014. The intraflagellar transport dynein complex of trypanosomes is made of a heterodimer of dynein heavy chains and of light and intermediate chains of distinct functions. *Mol. Biol. Cell.* 25:2620–2633. https://doi.org/10.1091/mbc.e14-05-0961

Brenner, S. 1974. The genetics of Caenorhabditis elegans. *Genetics.* 77:71–94. https://doi.org/10.1093/genetics/77.1.71

Cornils, A., A.K. Maurya, L. Tereshko, J. Kennedy, A.G. Brear, V. Prahlad, O.E. Blacque, and P. Sengupta. 2016. Structural and Functional Recovery of Sensory Cilia in C. elegans IFT Mutants upon Aging. *PLoS Genet.* 12:e1006325. https://doi.org/10.1371/journal.pgen.1006325

Cossu, C., F. Incani, M.L. Serra, A. Coiana, G. Crisponi, L. Boccone, and M.C. Rosatelli. 2016. New mutations in DYNC2H1 and WDR60 genes revealed by whole-exome sequencing in two unrelated Sardinian families with Jeune asphyxiating thoracic dystrophy. *Clin. Chim. Acta.* 455:172–180. https://doi.org/10.1016/j.cca.2016.02.006

Dagoneau, N., M. Goulet, D. Geneviève, Y. Sznajer, J. Martinovic, S. Smithson, C. Huber, G. Baujat, E. Flori, L. Tecco, et al. 2009. DYNC2H1 mutations cause asphyxiating thoracic dystrophy and short rib-polydactyly syndrome, type III. *Am. J. Hum. Genet.* 84:706–711. https://doi.org/10.1016/j.ajhg.2009.04.016

Dokshin, G.A., K.S. Ghanta, K.M. Piscopo, and C.C. Mello. 2018. Robust Genome Editing with Short Single-Stranded and Long, Partially Single-Stranded DNA Donors in *Caenorhabditis elegans*. *Genetics.* 210:781–787. https://doi.org/10.1534/genetics.118.301532

Drummond, I.A. 2012. Cilia functions in development. *Curr. Opin. Cell Biol.* 24:24–30. https://doi.org/10.1016/j.ceb.2011.12.007

Garcia-Gonzalo, F.R., and J.F. Reiter. 2017. Open Sesame: How Transition Fibers and the Transition Zone Control Ciliary Composition. *Cold Spring Harb. Perspect. Biol.* 9:a028134. https://doi.org/10.1101/cshperspect.a028134

Hamada, Y., Y. Tsurumi, S. Nozaki, Y. Katoh, and K. Nakayama. 2018. Interaction of WDR60 intermediate chain with TCTEX1D2 light chain of the dynein-2 complex is crucial for ciliary protein trafficking. *Mol. Biol. Cell.* 29:1628–1639. https://doi.org/10.1091/mbc.E18-03-0173

Hou, Y., and G.B. Witman. 2015. Dynein and intraflagellar transport. *Exp. Cell Res.* 334:26–34. https://doi.org/10.1016/j.yexcr.2015.02.017

Hou, Y., G.J. Pazour, and G.B. Witman. 2004. A dynein light intermediate chain, D1bLIC, is required for retrograde intraflagellar transport. *Mol. Biol. Cell.* 15:4382–4394. https://doi.org/10.1091/mbc.e04-05-0377

Huangfu, D., and K.V. Anderson. 2005. Cilia and Hedgehog responsiveness in the mouse. *Proc. Natl. Acad. Sci. USA.* 102:11325–11330. https://doi.org/10.1073/pnas.0505328102

Huber, C., S. Wu, A.S. Kim, S. Sigaudy, A. Sarukhanov, V. Serre, G. Baujat, K.H. Le Quan Sang, D.L. Rimoin, D.H. Cohn, et al. 2013. WDR34 mutations that cause short-rib polydactyly syndrome type III/severe asphyxiating thoracic dysplasia reveal a role for the NF-κB pathway in cilia. *Am. J. Hum. Genet.* 93:926–931. https://doi.org/10.1016/j.ajhg.2013.10.007

Jana, S.C., S. Mendonça, P. Machado, S. Werner, J. Rocha, A. Pereira, H. Maiato, and M. Bettencourt-Dias. 2018. Differential regulation of transition zone and centriole proteins contributes to ciliary base diversity. *Nat. Cell Biol.* 20:928–941. https://doi.org/10.1038/s41556-018-0132-1

Jauregui, A.R., K.C. Nguyen, D.H. Hall, and M.M. Barr. 2008. The Caenorhabditis elegans nephrocystins act as global modifiers of cilium structure. *J. Cell Biol.* 180:973–988. https://doi.org/10.1083/jcb.200707090

Jensen, V.L., C. Li, R.V. Bowie, L. Clarke, S. Mohan, O.E. Blacque, and M.R. Leroux. 2015. Formation of the transition zone by Mks5/Rpgrip1L establishes a ciliary zone of exclusion (CIZE) that compartmentalises ciliary signalling proteins and controls PIP2 ciliary abundance. *EMBO J.* 34:2537–2556. https://doi.org/10.15252/embj.201488044

Jensen, V.L., N.J. Lambacher, C. Li, S. Mohan, C.L. Williams, P.N. Inglis, B.K. Yoder, O.E. Blacque, and M.R. Leroux. 2018. Role for intraflagellar transport in building a functional transition zone. *EMBO Rep.* 19:e45862. https://doi.org/10.15252/embr.201845862

Kakar, N., D. Horn, E. Decker, N. Sowada, C. Kubisch, J. Ahmad, G. Borck, and C. Bergmann. 2018. Expanding the phenotype associated with biallelic WDR60 mutations: Siblings with retinal degeneration and polydactyly lacking other features of short rib thoracic dystrophies. *Am. J. Med. Genet. A.* 176:438–442. https://doi.org/10.1002/ajmg.a.38562

Kozminski, K.G., K.A. Johnson, P. Forscher, and J.L. Rosenbaum. 1993. A motility in the eukaryotic flagellum unrelated to flagellar beating. *Proc. Natl. Acad. Sci. USA.* 90:5519–5523. https://doi.org/10.1073/pnas.90.12.5519

Kozminski, K.G., P.L. Beech, and J.L. Rosenbaum. 1995. The Chlamydomonas kinesin-like protein FLA10 is involved in motility associated with the flagellar membrane. *J. Cell Biol.* 131:1517–1527. https://doi.org/10.1083/jcb.131.6.1517

Downloaded from http://rupress.org/jcb/article-pdf/221/1/e202010178/1818538/jcb_202010178.pdf by guest on 10 February 2026

Lambacher, N.J., A.L. Bruel, T.J. van Dam, K. Szymańska, G.G. Slaats, S. Kuhns, G.J. McManus, J.E. Kennedy, K. Gaff, K.M. Wu, et al. 2016. TMEM107 recruits ciliopathy proteins to subdomains of the ciliary transition zone and causes Joubert syndrome. *Nat. Cell Biol.* 18:122–131. https://doi.org/10.1038/ncb3273

Li, C., V.L. Jensen, K. Park, J. Kennedy, F.R. Garcia-Gonzalo, M. Romani, R. De Mori, A.L. Bruel, D. Gaillard, B. Doray, et al. 2016. MKS5 and CEP290 Dependent Assembly Pathway of the Ciliary Transition Zone. *PLoS Biol.* 14:e1002416. https://doi.org/10.1371/journal.pbio.1002416

Mangeol, P., B. Prevo, and E.J. Peterman. 2016. KymographClear and KymographDirect: two tools for the automated quantitative analysis of molecular and cellular dynamics using kymographs. *Mol. Biol. Cell.* 27: 1948–1957. https://doi.org/10.1091/mbc.e15-06-0404

May, S.R., A.M. Ashique, M. Karlen, B. Wang, Y. Shen, K. Zarbalis, J. Reiter, J. Ericson, and A.S. Peterson. 2005. Loss of the retrograde motor for IFT disrupts localization of Smo to cilia and prevents the expression of both activator and repressor functions of Gli. *Dev. Biol.* 287:378–389. https://doi.org/10.1016/j.ydbio.2005.08.050

McInerney-Leo, A.M., M. Schmidts, C.R. Cortés, P.J. Leo, B. Gener, A.D. Courtney, B. Gardiner, J.A. Harris, Y. Lu, M. Marshall, et al. UK10K Consortium. 2013. Short-rib polydactyly and Jeune syndromes are caused by mutations in WDR60. *Am. J. Hum. Genet.* 93:515–523. https://doi.org/10.1016/j.ajhg.2013.06.022

Merrill, A.E., B. Merriman, C. Farrington-Rock, N. Camacho, E.T. Sebald, V.A. Funari, M.J. Schibler, M.H. Firestein, Z.A. Cohn, M.A. Priore, et al. 2009. Ciliary abnormalities due to defects in the retrograde transport protein DYNC2H1 in short-rib polydactyly syndrome. *Am. J. Hum. Genet.* 84:542–549. https://doi.org/10.1016/j.ajhg.2009.03.015

Mijalkovic, J., B. Prevo, F. Oswald, P. Mangeol, and E.J. Peterman. 2017. Ensemble and single-molecule dynamics of IFT dynein in Caenorhabditis elegans cilia. *Nat. Commun.* 8:14591. https://doi.org/10.1038/ncomms14591

Mikami, A., S.H. Tynan, T. Hama, K. Luby-Phelps, T. Saito, J.E. Crandall, J.C. Besharse, and R.B. Vallee. 2002. Molecular structure of cytoplasmic dynein 2 and its distribution in neuronal and ciliated cells. *J. Cell Sci.* 115: 4801–4808. https://doi.org/10.1242/jcs.00168

Nachury, M.V., and D.U. Mick. 2019. Establishing and regulating the composition of cilia for signal transduction. *Nat. Rev. Mol. Cell Biol.* 20: 389–405. https://doi.org/10.1038/s41580-019-0116-4

Niceta, M., K. Margiotti, M.C. Digilio, V. Guida, A. Bruselles, S. Pizzi, A. Ferraris, L. Memo, N. Laforgia, M.L. Dentici, et al. 2018. Biallelic mutations in DYNC2LI1 are a rare cause of Ellis-van Creveld syndrome. *Clin. Genet.* 93:632–639. https://doi.org/10.1111/cge.13128

Oswald, F., B. Prevo, S. Acar, and E.J.G. Peterman. 2018. Interplay between Ciliary Ultrastructure and IFT-Train Dynamics Revealed by Single-Molecule Super-resolution Imaging. *Cell Rep.* 25:224–235. https://doi.org/10.1016/j.celrep.2018.09.019

Patel-King, R.S., R.M. Gilberti, E.F. Hom, and S.M. King. 2013. WD60/FAP163 is a dynein intermediate chain required for retrograde intraflagellar transport in cilia. *Mol. Biol. Cell.* 24:2668–2677. https://doi.org/10.1091/mbc.e13-05-0266

Pazour, G.J., B.L. Dickert, and G.B. Witman. 1999. The DHC1b (DHC2) isoform of cytoplasmic dynein is required for flagellar assembly. *J. Cell Biol.* 144: 473–481. https://doi.org/10.1083/jcb.144.3.473

Porter, M.E., R. Bower, J.A. Knott, P. Byrd, and W. Dentler. 1999. Cytoplasmic dynein heavy chain 1b is required for flagellar assembly in Chlamydomonas. *Mol. Biol. Cell.* 10:693–712. https://doi.org/10.1091/mbc.10.3.693

Prevo, B., P. Mangeol, F. Oswald, J.M. Scholey, and E.J. Peterman. 2015. Functional differentiation of cooperating kinesin-2 motors orchestrates cargo import and transport in C. elegans cilia. *Nat. Cell Biol.* 17: 1536–1545. https://doi.org/10.1038/ncb3263

Prevo, B., J.M. Scholey, and E.J.G. Peterman. 2017. Intraflagellar transport: mechanisms of motor action, cooperation, and cargo delivery. *FEBS J.* 284:2905–2931. https://doi.org/10.1111/febs.14068

Rana, A.A., J.P. Barbera, T.A. Rodriguez, D. Lynch, E. Hirst, J.C. Smith, and R.S. Beddington. 2004. Targeted deletion of the novel cytoplasmic dynein mD2LIC disrupts the embryonic organiser, formation of the body axes and specification of ventral cell fates. *Development.* 131: 4999–5007. https://doi.org/10.1242/dev.01389

Reck, J., A.M. Schauer, K. VanderWaal Mills, R. Bower, D. Tritschler, C.A. Perrone, and M.E. Porter. 2016. The role of the dynein light intermediate chain in retrograde IFT and flagellar function in Chlamydomonas. *Mol. Biol. Cell.* 27:2404–2422. https://doi.org/10.1091/mbc.e16-03-0191

Roberts, A.J. 2018. Emerging mechanisms of dynein transport in the cytoplasm versus the cilium. *Biochem. Soc. Trans.* 46:967–982. https://doi.org/10.1042/BST20170568

Rompolas, P., L.B. Pedersen, R.S. Patel-King, and S.M. King. 2007. Chlamydomonas FAP133 is a dynein intermediate chain associated with the retrograde intraflagellar transport motor. *J. Cell Sci.* 120:3653–3665. https://doi.org/10.1242/jcs.012773

Sanders, A.A., J. Kennedy, and O.E. Blacque. 2015. Image analysis of Caenorhabditis elegans ciliary transition zone structure, ultrastructure, molecular composition, and function. *Methods Cell Biol.* 127:323–347. https://doi.org/10.1016/bs.mcb.2015.01.010

Schafer, J.C., C.J. Haycraft, J.H. Thomas, B.K. Yoder, and P. Swoboda. 2003. XBX-1 encodes a dynein light intermediate chain required for retrograde intraflagellar transport and cilia assembly in Caenorhabditis elegans. *Mol. Biol. Cell.* 14:2057–2070. https://doi.org/10.1091/mbc.e02-10-0677

Scheidel, N., and O.E. Blacque. 2018. Intraflagellar Transport Complex A Genes Differentially Regulate Cilium Formation and Transition Zone Gating. *Curr. Biol.* 28:3279–3287.e2. https://doi.org/10.1016/j.cub.2018.08.017

Schmidts, M., J. Vodopiutz, S. Christou-Savina, C.R. Cortés, A.M. McInerney-Leo, R.D. Emes, H.H. Arts, B. Tüysüz, J. D'Silva, P.J. Leo, et al. UK10K. 2013. Mutations in the gene encoding IFT dynein complex component WDR34 cause Jeune asphyxiating thoracic dystrophy. *Am. J. Hum. Genet.* 93:932–944. https://doi.org/10.1016/j.ajhg.2013.10.003

Schmidts, M., Y. Hou, C.R. Cortés, D.A. Mans, C. Huber, K. Boldt, M. Patel, J. van Reeuwijk, J.M. Plaza, S.E. van Beersum, et al. UK10K. 2015. TCTEX1D2 mutations underlie Jeune asphyxiating thoracic dystrophy with impaired retrograde intraflagellar transport. *Nat. Commun.* 6:7074. https://doi.org/10.1038/ncomms8074

Schouteden, C., D. Serwas, M. Palfy, and A. Dammermann. 2015. The ciliary transition zone functions in cell adhesion but is dispensable for axoneme assembly in C. elegans. *J. Cell Biol.* 210:35–44. https://doi.org/10.1083/jcb.201501013

Shih, S.M., B.D. Engel, F. Kocabas, T. Bilyard, A. Gennerich, W.F. Marshall, and A. Yildiz. 2013. Intraflagellar transport drives flagellar surface motility. *eLife.* 2:e00744. https://doi.org/10.7554/eLife.00744

Swoboda, P., H.T. Adler, and J.H. Thomas. 2000. The RFX-type transcription factor DAF-19 regulates sensory neuron cilium formation in C. elegans. *Mol. Cell.* 5:411–421. https://doi.org/10.1016/S1097-2765(00)80436-0

Taylor, S.P., T.J. Dantas, I. Duran, S. Wu, R.S. Lachman, S.F. Nelson, D.H. Cohn, R.B. Vallee, and D. Krakow. University of Washington Center for Mendelian Genomics Consortium. 2015. Mutations in DYNC2LI1 disrupt cilia function and cause short rib polydactyly syndrome. *Nat. Commun.* 6:7092. https://doi.org/10.1038/ncomms8092

Toropova, K., M. Mladenov, and A.J. Roberts. 2017. Intraflagellar transport dynein is autoinhibited by trapping of its mechanical and track-binding elements. *Nat. Struct. Mol. Biol.* 24:461–468. https://doi.org/10.1038/nsmb.3391

Toropova, K., R. Zalyte, A.G. Mukhopadhyay, M. Mladenov, A.P. Carter, and A.J. Roberts. 2019. Structure of the dynein-2 complex and its assembly with intraflagellar transport trains. *Nat. Struct. Mol. Biol.* 26:823–829. https://doi.org/10.1038/s41594-019-0286-y

Tsurumi, Y., Y. Hamada, Y. Katoh, and K. Nakayama. 2019. Interactions of the dynein-2 intermediate chain WDR34 with the light chains are required for ciliary retrograde protein trafficking. *Mol. Biol. Cell.* 30:658–670. https://doi.org/10.1091/mbc.E18-10-0678

Vuolo, L., N.L. Stevenson, K.J. Heesom, and D.J. Stephens. 2018. Dynein-2 intermediate chains play crucial but distinct roles in primary cilia formation and function. *eLife.* 7:e39655. https://doi.org/10.7554/eLife.39655

Vuolo, L., N.L. Stevenson, A.G. Mukhopadhyay, A.J. Roberts, and D.J. Stephens. 2020. Cytoplasmic dynein-2 at a glance. *J. Cell Sci.* 133:jcs240614. https://doi.org/10.1242/jcs.240614

Webb, S., A.G. Mukhopadhyay, and A.J. Roberts. 2020. Intraflagellar transport trains and motors: Insights from structure. *Semin. Cell Dev. Biol.* 107:82–90. https://doi.org/10.1016/j.semcdb.2020.05.021

Wicks, S.R., C.J. de Vries, H.G. van Luenen, and R.H. Plasterk. 2000. CHE-3, a cytosolic dynein heavy chain, is required for sensory cilia structure and function in Caenorhabditis elegans. *Dev. Biol.* 221:295–307. https://doi.org/10.1006/dbio.2000.9686

Williams, C.L., C. Li, K. Kida, P.N. Inglis, S. Mohan, L. Semenec, N.J. Bialas, R.M. Stupay, N. Chen, O.E. Blacque, et al. 2011. MKS and NPHP modules cooperate to establish basal body/transition zone membrane associations

Downloaded from http://rupress.org/jcb/article-pdf/221/1/e202010178/1818538/jcb_202010178.pdf by guest on 10 February 2026

and ciliary gate function during ciliogenesis. *J. Cell Biol.* 192:1023–1041. https://doi.org/10.1083/jcb.201012116

Wu, C., J. Li, A. Peterson, K. Tao, and B. Wang. 2017. Loss of dynein-2 intermediate chain Wdr34 results in defects in retrograde ciliary protein trafficking and Hedgehog signaling in the mouse. *Hum. Mol. Genet.* 26: 2386–2397. https://doi.org/10.1093/hmg/ddx127

Yi, P., W.J. Li, M.Q. Dong, and G. Ou. 2017. Dynein-Driven Retrograde Intraflagellar Transport Is Triphasic in C. elegans Sensory Cilia. *Curr. Biol.* 27:1448–1461.e7. https://doi.org/10.1016/j.cub.2017.04.015

Zhu, X., J. Wang, S. Li, K. Lechtreck, and J. Pan. 2021. IFT54 directly interacts with kinesin-II and IFT dynein to regulate anterograde intraflagellar transport. *EMBO J.* 40:e105781. https://doi.org/10.15252/embj.2020105781

Downloaded from http://rupress.org/jcb/article-pdf/221/1/e202010178/1818538/jcb_202010178.pdf by guest on 10 February 2026

Supplemental material

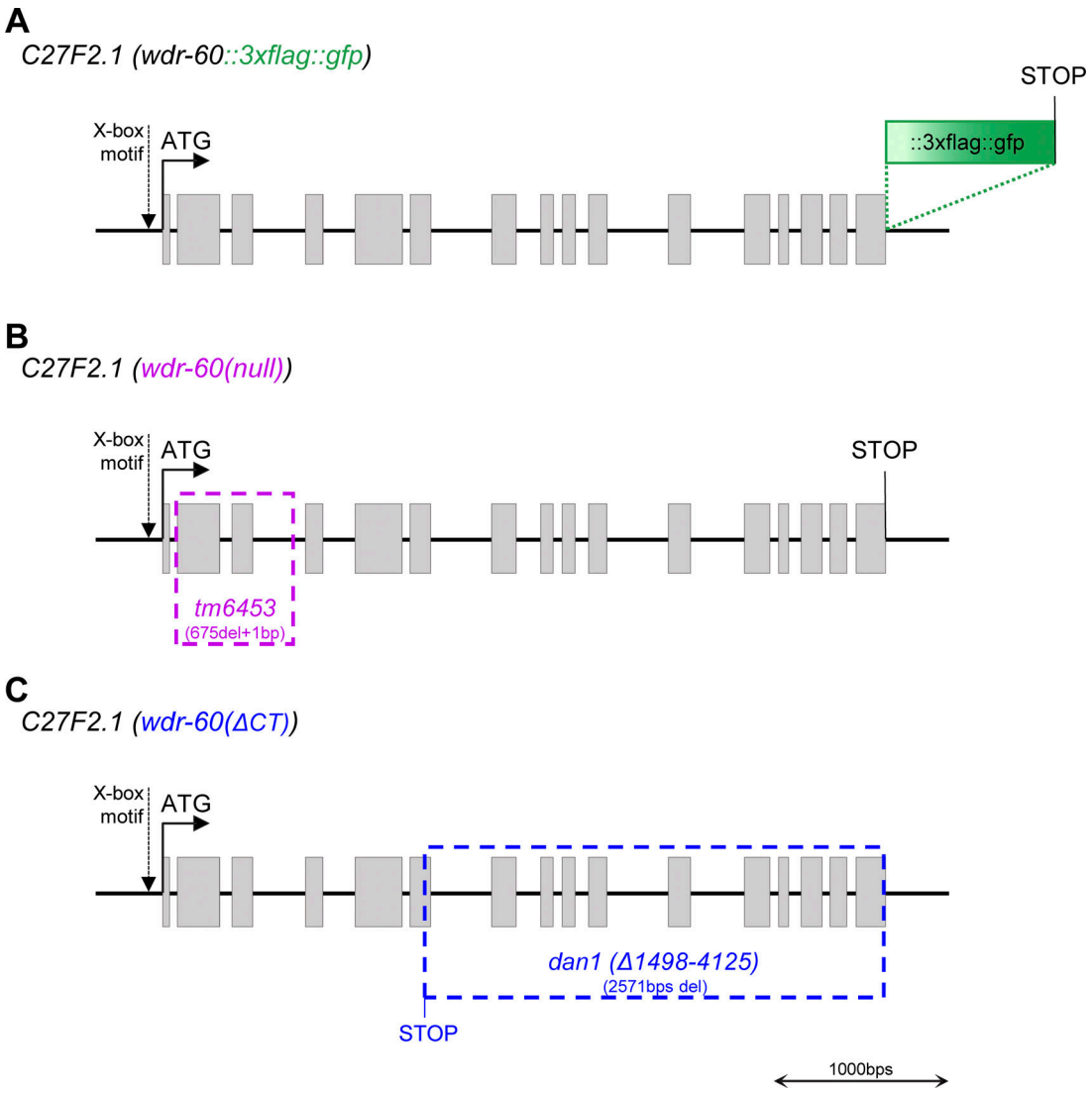

Figure S1. **Schematic of the *C27F2.1* locus organization in the *C. elegans* genome**. Related to Figs. 1 and 2. Predicted *wdr-60* exons (in gray boxes), including the start and stop codons, and the X-box motif according to Blacque et al. (2005). **(A)** Knock-in insertion of the *::3xflag::gfp* sequence at the 3′ end of the *wdr-60* genomic sequence (in-frame with the WDR-60 coding sequence). **(B)** Representation of the *wdr-60(tm6453)* null allele. **(C)** Representation of the *wdr-60(ΔCT)* allele (also named *dan1(Δ1498-4125 bps)*) corresponding to a WDR-60 truncation of the C-terminal β-propeller domain (Δ288–668 aa).

Downloaded from http://rupress.org/jcb/article-pdf/221/1/e202010178/1818538/jcb_202010178.pdf by guest on 10 February 2026

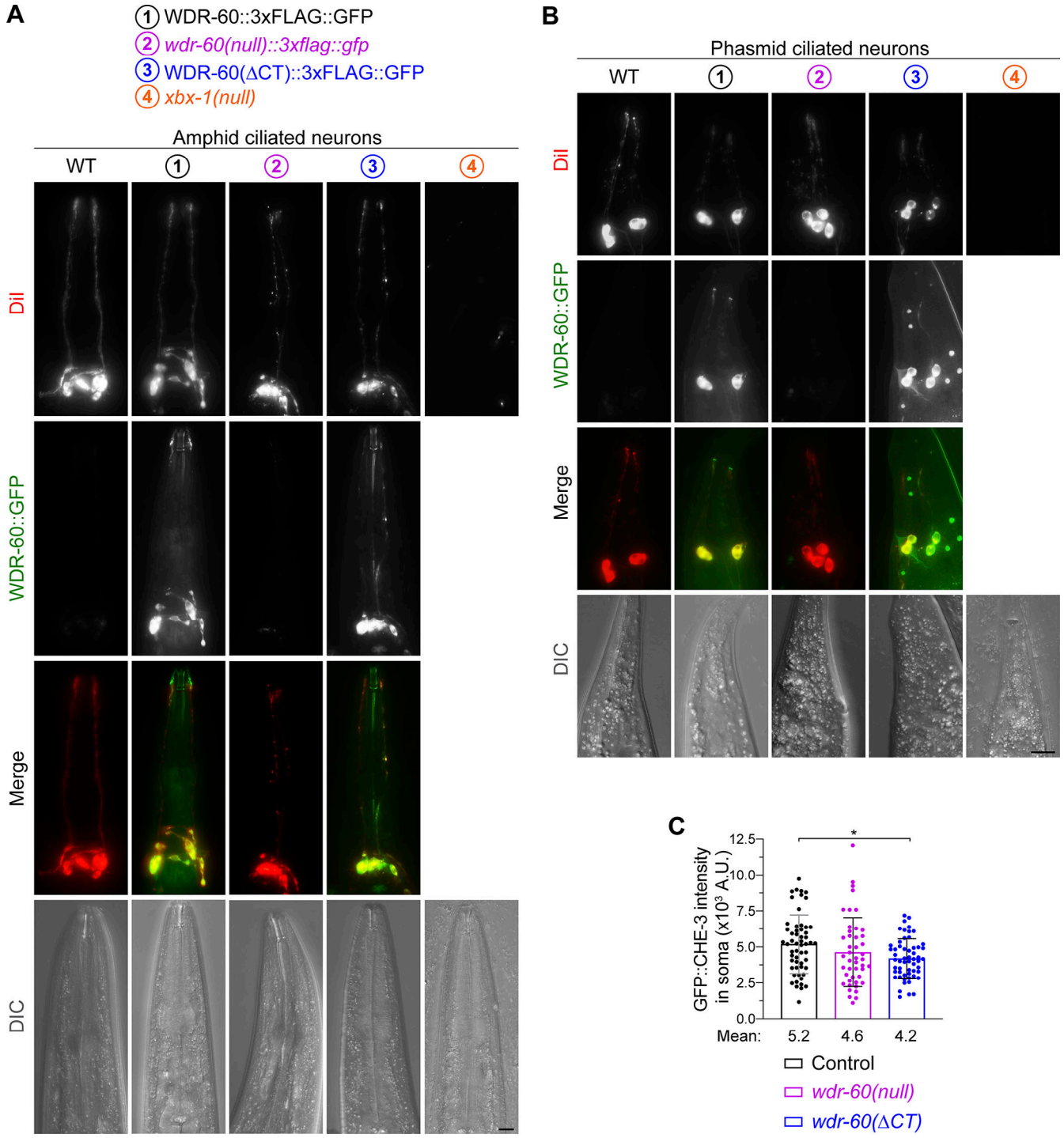

Figure S2. **WDR-60::3xFLAG::GFP expression is restricted to ciliated sensory neurons.** Related to Figs. 2 and 3. **(A and B)** Endogenously tagged WDR-60::3xFLAG::GFP and WDR-60(ΔCT)::3xFLAG::GFP are expressed in the same amphid (A) and phasmid (B) ciliated neurons that incorporate the DiI lipophilic dye (in red). The *wdr-60(null)::3xflag::gfp* strain has no detectable GFP signal in its neurons; however, they are still able to take up the DiI dye. Scale bars: 10 µm. DIC, differential interference contrast. **(C)** GFP::CHE-3 intensity in soma of phasmid sensory neurons of untagged *wdr-60* mutants ($n \geq 45$ somas). Graph is shown as mean ± SD. Kruskal–Wallis test followed by the Dunn's multiple comparison were used to analyze these datasets. *, $P \leq 0.05$.

Downloaded from http://rupress.org/jcb/article-pdf/221/1/e202010178/1818538/jcb_202010178.pdf by guest on 10 February 2026

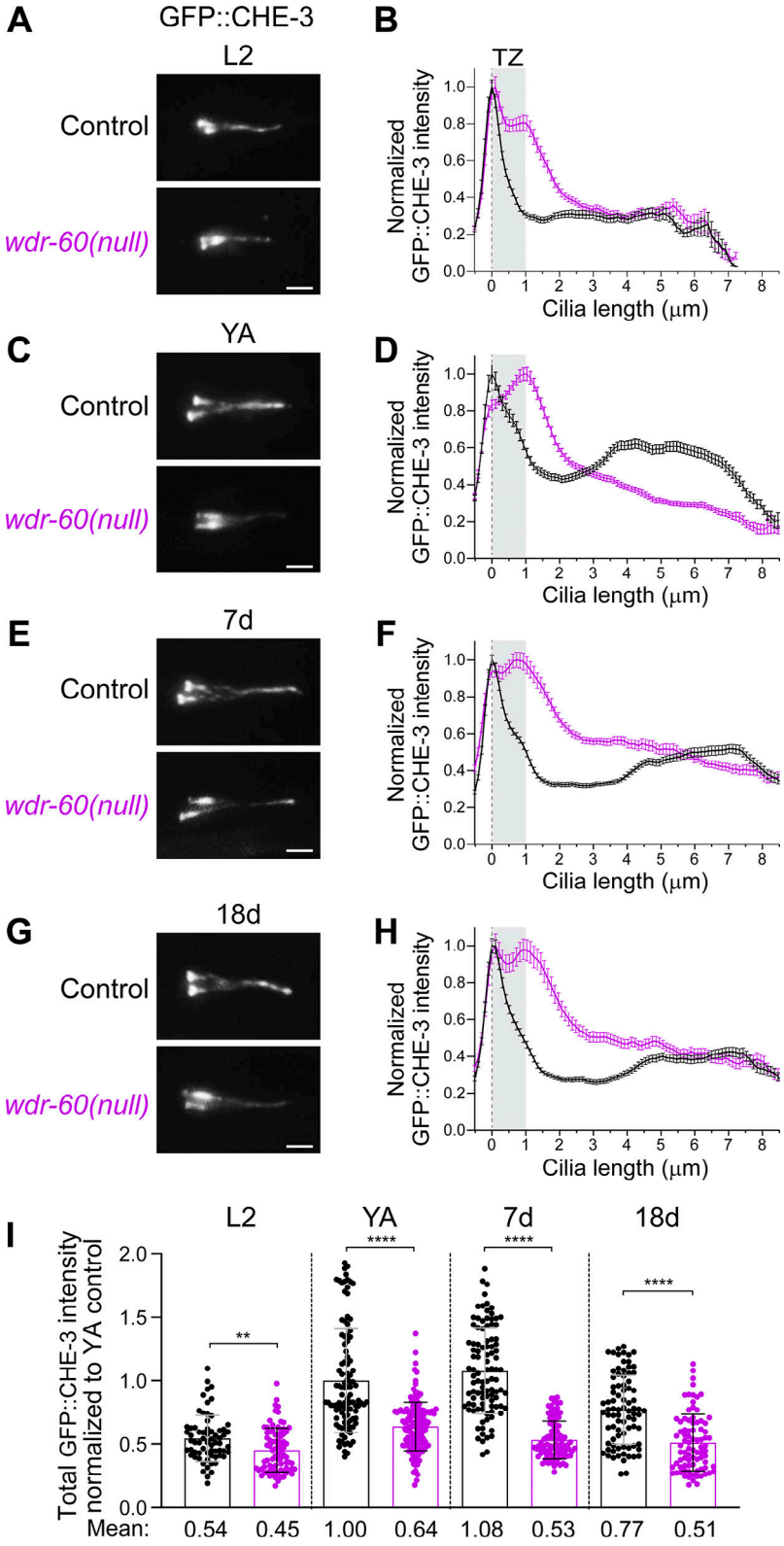

Figure S3. **WDR-60–associated phenotypes become worse as the animals develop to adulthood and do not improve with aging.** Related to Fig. 3. **(A, C, E, and G)** GFP::CHE-3-expressing phasmid cilia of wild-type and *wdr-60(null)* mutants at several stages of development and aging. L2, larval stage 2 worms; YA:,young adult worms; 7d, worms 7 days after reaching adulthood; 18d, worms 18 days after reaching adulthood. Scale bars: 2 μm. **(B, D, F, and H)** Corresponding distribution of GFP::CHE-3 signal intensity along cilia. Gray rectangles highlight the TZ, as previously defined. n = 77 cilia for B, $n \geq 95$ cilia for D, $n \geq 113$ cilia for F, and $n \geq 110$ cilia for H. XY intensity distribution graphs are shown as mean ± SEM. **(I)** Column graph showing GFP::CHE-3 total intensity from the base to the tip of cilia from wild-type and *wdr-60(null)* mutants analyzed in B, C, F, and H. Graph is shown as mean ± SD. Mann–Whitney *U* test was used to analyze these datasets. **, P ≤ 0.01; ****, P ≤ 0.0001.

Downloaded from http://rupress.org/jcb/article-pdf/221/1/e202010178/1818538/jcb_202010178.pdf by guest on 10 February 2026

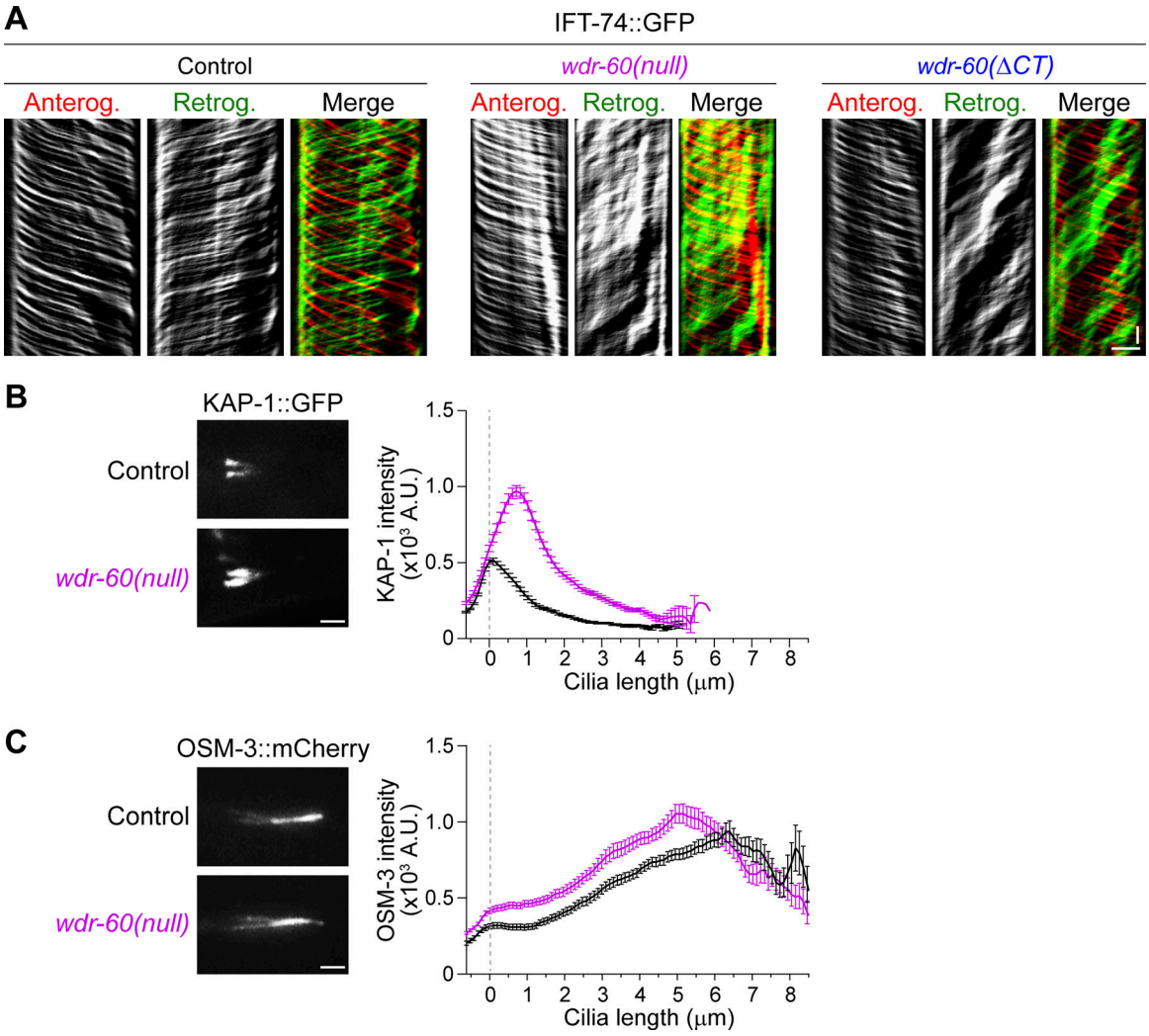

Figure S4. **Loss of WDR-60 results in a severe accumulation of KAP-1 near the base of cilia but only has a modest effect on the distribution of OSM-3.** Related to Fig. 4. **(A)** IFT-74::GFP kymographs of a phasmid cilia from control and *wdr-60(null)* worms. Single channels of particles moving anterogradely and retrogradely are shown, together with their respective merge. **(B)** Examples of phasmid cilia from control and *wdr-60(null)* worms expressing KAP-1::GFP and quantification of the signal intensity along cilia ($n \geq 60$ cilia for each strain). The intensity of KAP-1::GFP in cilia is significantly increased in the *wdr-60(null)* mutant with particles accumulating near the TZ. **(C)** Examples of phasmid cilia from control and *wdr-60(null)* worms expressing OSM-3::mCherry and quantification of the signal intensity along cilia ($n \geq 88$ cilia for each strain). OSM-3::mCherry distribution and intensity along the cilium is only slightly altered in the *wdr-60(null)* mutant. XY intensity distribution graphs are shown as mean ± SEM. Scale bars: vertical 5 s, horizontal 2 μm (A); 2 μm (B and C).

Downloaded from http://rupress.org/jcb/article-pdf/221/1/e202010178/1818538/jcb_202010178.pdf by guest on 10 February 2026

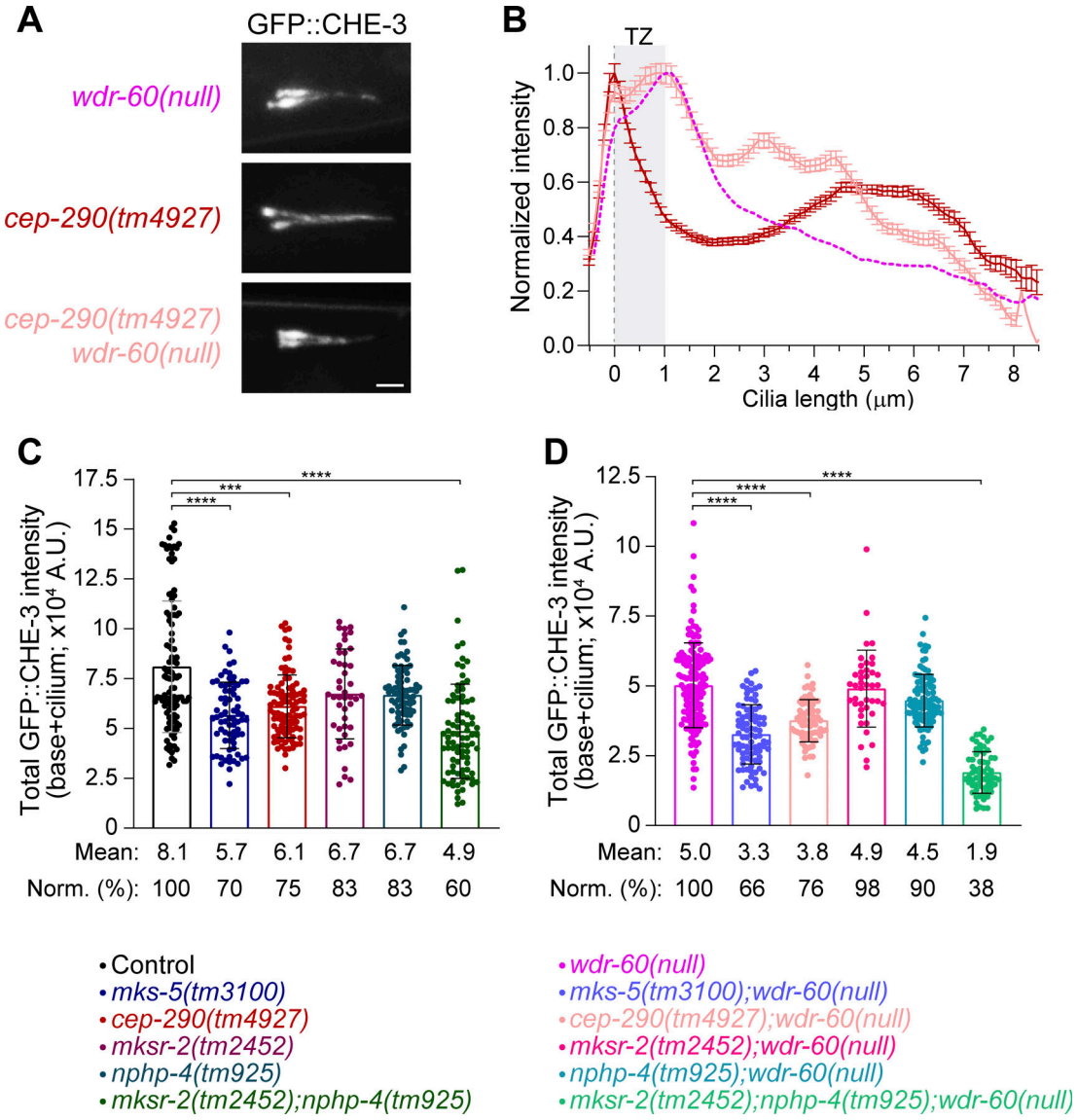

Figure S5. **Disruption of some TZ components changes the average levels of ciliary dynein-2.** Related to Fig. 7. **(A)** Phasmid cilia of the indicated *wdr-60* and *cep-290* mutant genotypes, expressing GFP::CHE-3. Scale bar: 2 μm. **(B)** Distribution of GFP::CHE-3 signal intensity along cilia from the strains in A ($n \geq 74$ cilia). The gray rectangle highlights the TZ, as previously defined. XY intensity distribution graph is shown as mean ± SEM. **(C and D)** Total GFP::CHE-3 intensity from the base to the tip of cilia from TZ mutants of the indicated genotypes, in wild-type *wdr-60* (C) and *wdr-60(null)* mutant (D) backgrounds. The cilia quantified here correspond to the same that were used to quantify the GFP::CHE-3 distribution profiles depicted in Fig. 7. Column graphs are shown as mean ± SD. Kruskal–Wallis test followed by Dunn's multiple comparison were used to analyze these datasets. ***, $P \leq 0.001$; ****, $P \leq 0.0001$.

Downloaded from http://rupress.org/jcb/article-pdf/221/1/e202010178/1818538/jcb_202010178.pdf by guest on 10 February 2026

Video 1. **Live imaging of GFP::CHE-3 (top) and WDR-60::GFP (bottom) undergoing IFT in *C. elegans* phasmid cilia.** Related to Fig. 1. Images were acquired at 3 fps, and playback is set at 15 fps (5× speed). Scale bar: 2 µm. The timer counts min:s.

Video 2. **Live imaging of GFP::CHE-3 in *C. elegans* phasmid cilia from control (top), *wdr-60(null)* (center), and *wdr-60(ΔCT)* (bottom) strains.** Related to Fig. 3. Images were acquired at 3 fps, and playback is set at 15 fps (5× speed). Scale bar: 2 µm. The timer counts min:s.

Video 3. **Live imaging of CHE-11::mCherry in *C. elegans* phasmid cilia from control (top), *wdr-60(null)* (center), and *wdr-60(ΔCT)* (bottom) strains.** Related to Fig. 4. Scale bar, 2 µm. Images were acquired at 3 fps, and playback is set at 15 fps (5× speed). Scale bar: 2 µm. The timer counts min:s.

Video 4. **Live imaging of IFT-74::GFP in *C. elegans* phasmid cilia from control (top), *wdr-60(null)* (center), and *wdr-60(ΔCT)* (bottom) strains.** Related to Figs. 4 and S4. Images were acquired at 3 fps, and playback is set at 15 fps (5× speed). Scale bar: 2 µm. The timer counts min:s.

Video 5. **Live imaging of GFP::CHE-3(K2935Q) in *C. elegans* phasmid cilia from control (top); *mks-5(tm3100)* (center), and *nphp-4(tm925)* (bottom) strains.** Related to Fig. 8. Images were acquired at 3 fps, and playback is set at 15 fps (5× speed). Scale bar: 2 µm. The timer counts min:s.

Video 6. **Live imaging of GFP::CHE-3 in *C. elegans* phasmid cilia from control (top), *mks-5(tm3100)* (center), and *nphp-4(tm925)* (bottom) strains.** Related to Fig. 9. Images were acquired at 3 fps, and playback is set at 15 fps (5× speed). Scale bar: 2 µm. The timer counts min:s.

Video 7. **Live imaging of GFP::CHE-3 in *C. elegans* phasmid cilia from *wdr-60(null)* (top), *wdr-60(null);mks-5(tm3100)* (center), and *wdr-60(null);nphp-4(tm925)* (bottom) strains.** Related to Fig. 9. Images were acquired at 3 fps, and playback is set at 15 fps (5× speed). Scale bar: 2 µm. The timer counts min:s.

Provided online are three tables. Table S1 shows the nomenclature of *C. elegans* proteins mentioned in the text and their corresponding homologues or orthologues in humans. Table S2 lists the strains used in this study. Table S3 lists the primers used in this study.

Downloaded from http://rupress.org/jcb/article-pdf/221/1/e202010178/1818538/jcb_202010178.pdf by guest on 10 February 2026